Next Materials 9 (2025) 101081

Contents lists available at ScienceDirect

Next Materials

journal homepage: www.sciencedirect.com/journal/next-materials

Research article

Carrier transport and induced magnetism in nanostructured carbon-based material manufactured by PECVD method

A.A. Kharchanka *, A.K. Fedotov, J.A. Fedotova

Institute for Nuclear Problems, Belarusian State University, 220006, Bobruiskaya str., 11, Minsk, Belarus

ARTICLE INFO

Keywords:
Carbon-based nanolayers
Charge carrier transport mechanisms
Induced magnetism
Magnetotransport
Anomalous magnetoresistance

ABSTRACT

We studied sheet magnetoresistivity (*MR*) $R_{\square}(T,\mathbf{B})$ at $2 \le T \le 300$ K in magnetic fields $\mathbf{B} \le 8$ T in carbon-based nanolayers with islands of vertical graphene (*VG*) phase on their surface. Nanolayers with 20 and 35 nm thickness were accordingly deposited during 20 (*CBNL*20) and 40 (*CBNL*40) minutes on glass substrate by *PECVD* method. *MR* curves for *CBNL*20 sample with out-of-plane **B** orientation included contributions conditioned by 3 mechanisms: (i) 2*D* weak localization (WL) quantum corrections, (ii) free electrons scattering on (para)magnetic defects, and (iii) Lorentz-like (III). The $R_{\square}(T,\mathbf{B})$ dependences for 35 nm thick *CBNL*40 sample indicated the absence of mechanism (ii) i.e. lowering of spin-related charge carrier scattering. To agree negative magnetoresistance (*NMR*) effect with WL theory in high external **B** in *CBNL*40, we are forced to propose highly inhomogeneous distribution of (para)magnetic defects with uncompensated spins the most of which are formed under *VG* phase islands. The formed in this case ferromagnetic moments resulted in strong redistribution of magnetic flux Φ along C-layer plane: strong Φ weakening between islands and concentration of Φ near *VG* phase islands. This explains why we observe WL *NMR* effect in formally strong external **B** values while real **B** in C-layer is very low.

1. Introduction

Graphene- and carbon-based structures attract much attention from researchers due to the strong influence of growth methods on their electrical and other properties. The crystal-structural form of the carbon layers also has a significant impact on the properties of this type of carbon-based materials: amorphous, single-crystalline, polycrystalline with small and large grains (including nanosized), natural graphite, kish graphite, highly oriented pyrolytic graphite, etc. [1–5]. The variety of properties of carbon-based materials including their nanosized modifications (for example, single-sheet graphene [6], the so-called vertical graphene [7–12], graphite nanolayers, and other carbon structures) allows us to hope to use hybrid nanostructures based on graphite-like materials for sensors, solar cells, and electronic devices [13–16], energy storage devices [7–10], etc. In addition, graphite is used extensively in nuclear reactors [17,18], and electrodes in dry batteries. It serves as reinforcement in steels and has applications in anti-corrosion layers, etc.

The specific influence of temperature and magnetic field on the behavior of electric properties of graphite is due to its specific crystallographic structure. In crystalline graphite carbon valence electrons form sp^2 hybrid orbits, three of the four electrons bond the atoms into a planar hexagonal network in the plane, while the remaining electrons form a π-type molecular orbitals. Weak Van-der-Waals bonding in the interplanar c direction holds the layers together [1,2]. As a result, crystalline graphite is the unique elemental semimetal due to its extremal anisotropy with very small electron and hole carrier densities ($n \approx p \approx 3 \times 10^{18}$ cm^{-3}). The in-plane carrier effective masses (m^*) are very light ($\approx 0.05 m_e$), whereas those for interplane motion are about $10 m_e$, giving an enhancement of the density of electron states at the Fermi level [1]. Just due to its layered structure, crystalline graphite offers interesting perspectives to investigate magnetoresistive and Hall effects in low-dimensional structures.

An important feature of many carbon nanostructures (including graphite-like) is the ability to grow them directly on dielectric substrates. This eliminates the procedure for their transfer, for example, from a catalytic metal foil (copper, nickel, etc.), which is forced to be used in graphene technology [19].

The literature contains an abundance of scientific articles devoted to the preparation and study of the correlations between the structure and applied properties of graphite-like nanostructures (see [2–4,20–24] and references to them). However, in relation to electric properties of such materials, there is still no complete understanding of these relationships. Furthermore, there is still no complete understanding and

* Corresponding author.
E-mail addresses: xaatm@mail.ru (A.A. Kharchanka), akf1942@gmail.com (A.K. Fedotov), julia@hep.by (J.A. Fedotova).

https://doi.org/10.1016/j.nxmate.2025.101081
Received 14 June 2025; Received in revised form 14 August 2025; Accepted 15 August 2025
Available online 1 September 2025

satisfactory explanation of some "strange" features of charge carrier transport in these classes of materials in a magnetic field.

One of these problematic issues is the nature of the occurrence of the negative magnetoresistive (*NMR*) effect, which consists of an increase in conductivity with increasing magnetic field with induction **B** in graphite-like and some other carbon-based materials. In many works for graphite and polycrystalline single and multilayer CVD graphene [5,13,25–30]), this effect is interpreted on the basis of the theory of quantum corrections to the Drude conductivity [3,31–34] caused by phases breaking of wave functions of electrons when they move under conditions of the so called weak localization (WL) by self-crossing trajectories. However, this interpretation does not take into account that, according to the theory, quantum corrections should be suppressed already in very weak magnetic fields (no higher than 50...100 mT). Therefore, the use of this model to explain this strange *NMR* effect in strong magnetic fields (from 1 to 8 T) is not entirely understandable [5,35].

The second feature of graphite-like samples is associated with the observation of a linear (by field) positive magnetoresistive (*PMR*) effect [13,36], which is observed in the magnetic field **B** normal to the sample plane and electric current vector **I**. In contrast to the quadratic Lorentzian-like *PMR* effect, which saturates at fields much larger than the inverse of the carrier mobility [37], such a linear (non-saturated) behavior of the *PMR* and *NMR* effects (including at B up to 40...62 T) [2,38–44] cannot be explained from the point of view of the Lorentz force influence. Note that the linear behavior of $\Delta R(B) \sim B$ allows to obtain carbon-based structures for sensitive and inexpensive magnetic field sensors.

The third problematic issue is the simultaneous observation of *NMR* and *PMR* effects in two-dimensional samples with both their transverse and longitudinal orientations in a magnetic field. Note that in the latter case, vector **B** lies in the plane of the sample, but is still perpendicular to vector **I**. From the point of view of the classical band theory of the magnetoresistive effect, the Lorentzian contribution to the *PMR* in a longitudinal magnetic field should be absent (with rare exceptions) [37]. However, there is a set of materials or artificially created objects (and not only carbon-based) in which the longitudinal and transverse magnetoresistances are almost the same or very high. This behavior was explained by the influence of the Hall resistance, which increases linearly with the field increase when measuring the longitudinal *PMR* effect [36–39].

And finally, from the point of view of theories generally accepted to explain the *NMR* effect (for example, quantum corrections [45–47], hopping mechanism [48–50], distortion of current lines in compositions of high- and low-conducting phases when a magnetic field is applied [51]), the latter should fall with increasing temperature. However, experiments for a number of materials and structures indicate that the *NMR* remains unchanged with the temperature increase [39].

All of the above indicates that the behavior of electrical resistance in a magnetic field in carbon materials (especially highly inhomogeneous and/or heterogeneous) is far from understood. Therefore, this work is devoted to studying the features of carrier transport in two-phase carbon-based nanolayers (*CBNL*), consisting of a sublayer of defective graphite of nanometer thickness and nanosized islands (of different sizes and densities) of nucleus of vertical graphene (*VG*) phase.

2. Experimental

The formation of *CBNL* was carried out by microwave plasma-enhanced chemical vapor deposition (*PECVD*) at the IPLAS Innovative Plasma Systems GmbH installation. This technology in works [7–12] was used to grow nanosheets of vertical graphene. Details of experiments in our case were described in [52–54].

The structures were formed on fused silica substrates, which were pre-treated in hydrogen plasma with its flow rate of 200 cm^3/min and a microwave power of 1.2 kW to remove any organic residues, oxides and activate growth sites. After cleaning procedure, substrates were dried by N_2 flow substrates and then were loaded into the reactor. To produce two-phase *CBNL*, the substrate temperature was increased up to 850 ^oC (using substrate heater and remote plasma) and stabilized. After a 15 min process of the substrate preheating, methane gas was introduced into the reactor chamber at a flow rate of 50 cm^3/min for some time, and then the H_2 flow was reduced to 150 cm^3/min. The operating pressure was kept the same at 26 mbar during both preheating and the growth process.

We have studied samples *CBNL*20 and *CBNL*40 prepared by introducing methane gas into reactor chamber for 20 min and 40 min, respectively. The choice of the time of *CBNL* deposition on the substrate was based on the following ideas about the process of *VG* formation. According to works [7–12], at the first stage of *VG* phase formation, nanographite phase nuclei appear. In the second stage, these nuclei grow and merge into a thin and highly defective graphite sublayer containing point defects (such as pentagon and heptagon rings and others), completely covering the substrate. At the third stage, in the most defective zones of this sublayer, according to [7,11,12], the nucleation of islands of more perfect crystalline graphite occurs. At the fourth stage of growth, with an increase in the supply time of methane gas into the reactor chamber to more than 40 min, a *VG*-like structure is formed from these islands perpendicular to the substrate [7,11,12]. According to the task, the growth of *CBNL* in our experiments was stopped at the third stage. To study the properties, 3 samples of *CBNL*20 and *CBNL*40 were obtained in one synthesis. The obtained samples had a scattering of conductivity absolute values of no more than 20% and retained all the main behavioral features.

The crystallographic structure of *CBNL* samples was studied by Raman spectroscopy (RS) and scanning electron microscopy (*SEM*). RS measurements were carried out on a Nanofinder 30 device (Japan). The power of the laser beam with a wavelength of 532 nm and a diameter of about 0.7...1 μm was 600 μW with an irradiation time of 20 s. 3 areas with dimensions of 20 × 20 μm were scanned, spaced from each other at a distance of at least 1 mm. *SEM* studies of the sample surfaces were performed using an FEI Quanta 200 FEG instrument with a resolution of 1...2 nm, containing an electron field emission source in a Schottky-type electron gun. Cross-sectional *SEM* images were acquired using a Helios Nanolab 650 dual-beam system. It is important to keep in mind that a thin layer of Cr was deposited by magnetron sputtering on scanned area before *SEM* measurements.

Four-probe electric resistance R (conductance σ) as a function of temperature T and magnetic field with induction B applied normally or parallel to the samples surface was measured in the closed-cycle refrigerator system (CCRS), produced by Cryogenics Ltd (London), in the temperature range $2 < T < 300$ K and B values up to 8 T. Details of experiment were described earlier in [55,56]. Every time the vector of electric current **I** was perpendicular to vector **B**. The magnetic field is oriented with an accuracy of no worse than 0.1°. The relative magnetoresistance is defined as $MR = [R(B) - R(0)]/R(0)$, where $R(B)$ and $R(0)$ are resistances at non-zero and zero B values, accordingly. Measurements were performed on the samples with 4 indium (In) supersonically soldered electric contacts which were soldered by 50 μm diameter copper wires to the contact pad in a measuring cell. The cell with a sample on the contact pad was placed in a special measuring probe included LakeShore thermometers and magnetic field sensors, heaters, heated thermal shields, all in He gas atmosphere under low pressure. The probe was inserted into channel of superconducting solenoid inside the cryostat in CCRS. When studying the $R(T, \mathbf{B})$ or $\sigma(T, \mathbf{B})$ curves, the current through the sample was set and measured using a Keithley 6430 instrument, which made it possible to measure the electrical resistance of the samples in the range from 100 μΩ to 10 GΩ with an accuracy of no worse than 0.1%. Temperature was stabilized with the precision not less than 0.005 K using LakeShore 331 measuring controller. The accuracy of measuring the specific conductivity was no worse than 10%, which was mainly determined by the inaccuracy of measuring the geometric dimensions of the samples, the width of potential electrical contacts and the distances between them.

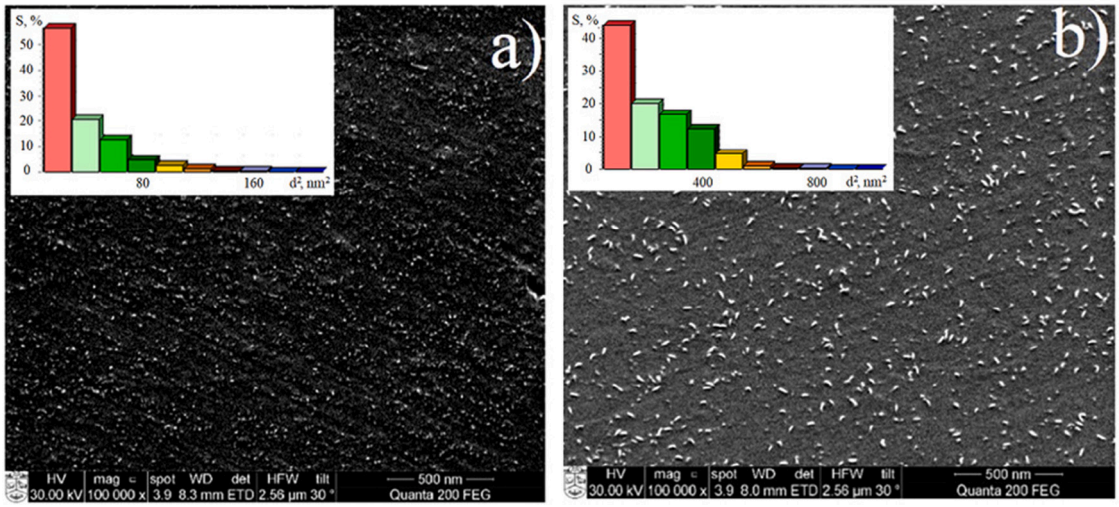

Fig. 1. *SEM* images of the surface for *CBNL*20 (a) and *CBNL*40 (b) samples in the backscattered electron mode. The insets show island area distributions obtained by image analysis using Autoscan2005 computer program. (For interpretation of the references to color in this figure legend, the reader is referred to the web version of this article.)

3. Results

3.1. Structure of carbon-based nanolayers

As mentioned above, the samples under study represent the precursor structures of vertical graphene (*VG*) described in works [7–10] at the initial stages of their formation, that is, carbon layers that arise before the direct formation of the *VG* phase. The surface of the samples under study presents homogeneous structures when studied both in optical and scanning microscopes. *SEM* images of the surface and cross-sections of *CBNL*20 (after a 20 min growth process) and *CBNL*40 (after a 40 min growth process) are presented in Figs. 1 and 2 (see also [52–54]).

As is seen in Fig. 1, *SEM* images of the surface of every *CBNL* sample look like a fairly uniform structure with a large number of stretched bright islands on top of a continuous carbon sublayer. Processing of *SEM* images using the Autoscan2005 computer program made it possible to estimate some dimensional parameters of bright islands and their density, representing that every island on the surface of each *CBNL* sample has an ellipse-like shape. From the distribution of these islands by area values, presented in the insets to Fig. 1a and b, it follows that in the sample *CBNL*20 approximately 56% of the area is occupied by islands with the smallest areas lying in the range of 1.5...27.7 nm^2, and for the sample *CBNL*40 about 44% of the islands occupy the area 1.36...123 nm^2. As can be seen from Table 1, the ratio of the areas occupied by bright areas to the area of the entire *SEM* image is about 0.77% for the *CBNL*20 sample and 1.08% for the *CBNL*40 sample, respectively. The change of growth time from 20 to 40 min leads to two consequences. On one side, an increase in the mean size of long and short axes of the elongated ellipse-like light areas (islands) is increased from ~4.2 nm to ~10.5 nm for long axes and from ~2.6 nm to ~6.1 nm for short axes, correspondingly, while their overlap does not occur. On the other side, the concentration of islands is strongly decreased from $2.5 \cdot 10^{10}$ cm^{-2} to $5.4 \cdot 10^{9}$ cm^{-2} for samples *CBNL*20 and *CBNL*40, accordingly. It is worth also noting that the formation of contrasting bright areas on *SEM* images of *CBNL* samples measured in the backscattered electron mode indicates the accumulation of charge in these areas. This fact, in turn, indicates a weak electrical interaction (the presence of barriers) between these areas and the general conductive carbon sublayer, which prevents charge drain from them. Therefore, these areas can be attributed to nuclei of future vertical *VG* phase in *VG* structures grown at longer times. In this case, the drop of islands' density after an increase of growth time can be attributed to either coalescence (due to incorporation of smaller *VG* phase nuclei by larger ones) or interrupting of low-sized *VG* phase nuclei growth (due to their overgrowing with a nanographitic layer) during the 40 min growth process.

Table 1
Dimension parameters of bright elongated islands (nuclei of *VG* phase) in *SEM* images of surface, thicknesses and $\sigma_{\square}$ of *CBNL*20 and *CBNL*40 samples.

Sample	*CBNL*20	*CBNL*40
Full square of processed *SEM* image, nm^2	$4.49 \cdot 10^{6}$	$1.84 \cdot 10^{7}$
Full number of islands (nuclei of *VG* phase) on processed *SEM* image	1040	999
Full square of islands (nuclei of *VG* phase) on processed *SEM* image, nm^2	$3.5 \cdot 10^{4}$	$2.0 \cdot 10^{5}$
Relation of islands' square to the processed *SEM* image square, %	0.774	1.084
Density of islands (nuclei of *VG* phase), cm^{-2}	$2.5 \cdot 10^{10}$	$5.4 \cdot 10^{9}$
Mean square of one island = πab, nm^2	34	200
Mean long axis α, nm	4.2	10.5
Mean short axis β, nm	2.6	6.1
Thicknesses, nm	20.3 ± 2.1	35.4 ± 4.9
$\sigma_{\square}$ at T = 300 K, Sm	$1.06 \cdot 10^{-4}$	$2.65 \cdot 10^{-4}$
$\sigma_{\square}$ at T = 2 K, Sm	$0.55 \cdot 10^{-4}$	$1.86 \cdot 10^{-4}$

As is seen from transverse chips in Fig. 2, in accordance with the growth scheme described above, both samples contain nanographitic C-layers with mean thicknesses of the order of 20.3 ± 2.1 and 35.4 ± 4.91 nm, respectively, on which we observe randomly distributed ellipse-like islands (nuclei) of graphite.

Fig. 3 show typical Raman spectra for both studied samples. They are practically do not change over the scanned area confirming the homogeneity of the samples' surface. The spectra show pronounced *G* and 2*D*-peaks indicating a structure characteristic for sp^2-hybridized carbon.

The presence of *D* and (*D*+*D*') lines in RS indicates the presence of a significant number of defects in the samples. The high intensity of the *G* and *D* peaks relative to the 2*D* peak confirms a fairly strong disorder of the structure, which is characteristic for the initial stages of growth of *VG* structures [7]. It is worth noting that the studied RS allowed us

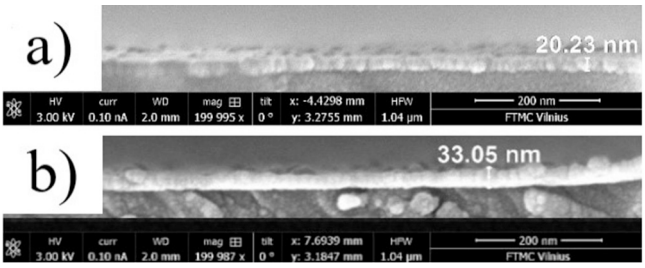

Fig. 2. Cross-section *SEM* images of *CBNL*20 (a) and *CBNL*40 (b) samples in the backscattered electron mode.

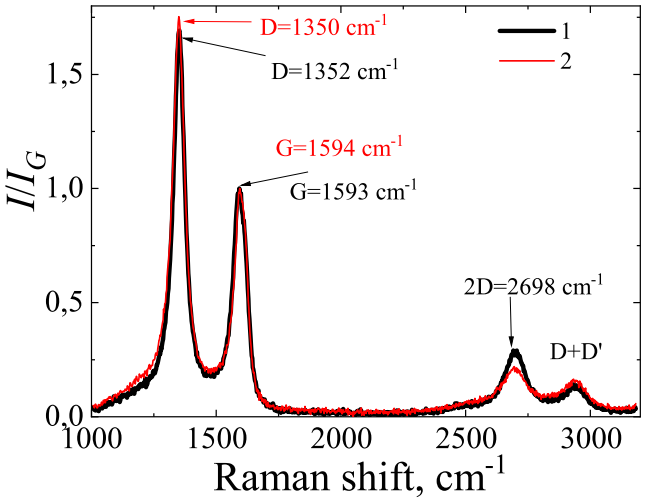

Fig. 3. An example of Raman spectra for samples *CBNL*20 (black line) and *CBNL*40 (red line). (For interpretation of the references to color in this figure legend, the reader is referred to the web version of this article.)

to detect only the presence of areas with sp^2 hybridization, although, as is known [11], such objects also have other carbon modifications.

Thus, in accordance with our and literature results, it can be assumed that the studied *CBNL* samples represent a defective graphite-like sublayer formed at the initial stages of the *PECVD* process, in which the appeared nuclei of future vertical graphene phase looked like islands with an elongated shape.

3.2. Electrical properties of CBNL samples in zero magnetic field

Let us note an important feature of measuring procedure when studying the temperature dependences of the conductivity (resistivity) of the *CBNL* samples. This feature was identified and described in details in our previous work [54] where we studied $\sigma(T, \mathbf{B})$ curves after a number of heating–cooling–heating cycles according to the procedure 300 K → 2 K → 300 K without and with removal of samples from cooled helium gas into air at 300 K. As was shown in [54], when stored in air at room temperature, the resistance of both samples practically did not change during time. However, an increase in resistance was noted during repeated thermal cycling in the temperature range of 2...300 K either in helium gas or when the samples were taken out into the air after heating up to 300 K. The results of this thermocycling will be described shortly below and in more detail in Supplemental Material A.

Before starting measurements of $\sigma(T)$ curves of the samples, their longitudinal current–voltage (I-V) characteristics were checked at temperatures T = 2 K and T = 300 K (inset in Fig. 4a. For both samples, the I-Vs turned out to be linear [54], which indicates the ohmic nature of the electrical contacts used. The higher resistance of the *CBNL*20 sample compared to the *CBNL*40 sample is most likely due to the smaller thickness and higher defectiveness of the conductive nanographitic sublayer in *CBNL*20 sample formed at the 20 min stage of the *PECVD* process.

As mentioned above, to understand the behavior of the $\sigma(T)$ dependencies, the samples were studied in process of 5-fold cooling–heating–cooling cycles [54]. Measurements during cycles N = 1...3 were carried out without removing the sample from the helium atmosphere into air after its last warming. After N = 3, the sample, after heating to 300 K, was taken out into the air for a short time (about 4...5 min) to change of the sample in the magnetic field, and then, after being placed in a helium atmosphere, two more cycles were carried out according to the scheme 300 K → 2 K → 300 K. Examples of $\sigma(T)$ curves in form for N = 1 and N = 5 see Supplemental Material A, Figure A.2.

Let us shortly discuss the mostly important features in the behavior of the σ curves depending on number N of thermal cycles. As was shown earlier in [54] and presented in Suppl. A, the σ depended on N with a tendency to saturation. At the same time, the increase in N had the greatest impact on the *CBNL*20 sample, where the decrease in $\sigma(T = 300\ \text{K})$ was close at 17% for N = 5 measuring cycle, while for the *CBNL*40 sample it did not exceed 1.6% under the same conditions. This behavior of the σ dependences and the observed "jumps" on $\sigma(T)$ curves (presented in Suppl. A and [54]) were explained by changes in the internal stresses in the samples during the cooling process due to the peculiarities of the formation of the nanographite sublayer. These changes most likely arose as a result of the rearrangement of defects formed at the grain boundaries and/or in the bulk of nanographite sublayer, and at the change of environmental atmosphere due to passivation of dangling bonds with atmospheric gases and water vapors. These stresses may also lead to ruptures (interstices) in the *CBNL* as they cool. As noted in [54], the role of defects in the sensitivity of electrical resistance to measurement modes can be supported by the fact that the *CBNL*40 sample, obtained with a longer deposition time, turned out to be significantly less sensitive to thermal cycling procedure (N value) than the *CBNL*20 sample. In [54] such behavior was attributed to a decrease in grain boundary stresses of the thicker graphite sublayer during the growth of nuclei of the vertical component of the *VG* phase.

In paper [54] (see Supplemental Material A), it was also shown that the temperature dependences of the conductance of *CBNL*20 had pronounced "jumps", which apparently reflect the restructuring of defects and possible breaks in the carbon structure. In this case, the number of "jumps" decreases significantly after several cycles of cooling//heating, but do not disappear completely, so in this sample temperature dependence of the $\sigma(T)/\sigma_{300}$ has a "jump" at a temperature $T \approx 131$ K, for this reason the analysis of this sample is divided into 2 sections, and for convenience, normalized conductivity values were used.

In general, in [54], similarity of $\sigma(T)/\sigma_{300}$ curves was observed at different N, which may indicate the conservation of the basic conductivity mechanisms of both samples at different stages of thermal cycling. To identify these mechanisms, detailed studies of the $\sigma(T, \mathbf{B})$ dependences were carried out during the last measuring cycle N = 5 at different orientations of magnetic field relative to the plane of the samples.

The behavior of the $\sigma(T)/\sigma_{300}$ curves (Fig. 4) demonstrate the semiconductor (close to exponential) nature of carrier transport in both samples. The most likely reasons for this behavior in carbon materials can be either activation mechanism [50,57]:

$$\sigma(T) \approx \sigma_0^D \cdot exp\left[-\left(\frac{T_0^D}{T}\right)^{\alpha}\right]. \quad (1)$$

where the model parameters α, σ_0^D and T_0^D characterize hopping conduction with a variable range hopping (*VRH*) depending on dimension (D = 1, 2 or 3) of the samples under study. These parameters allow to extract the energy dependence of the density of localized states along which the hopping of electrons occur. According to [48–50], the

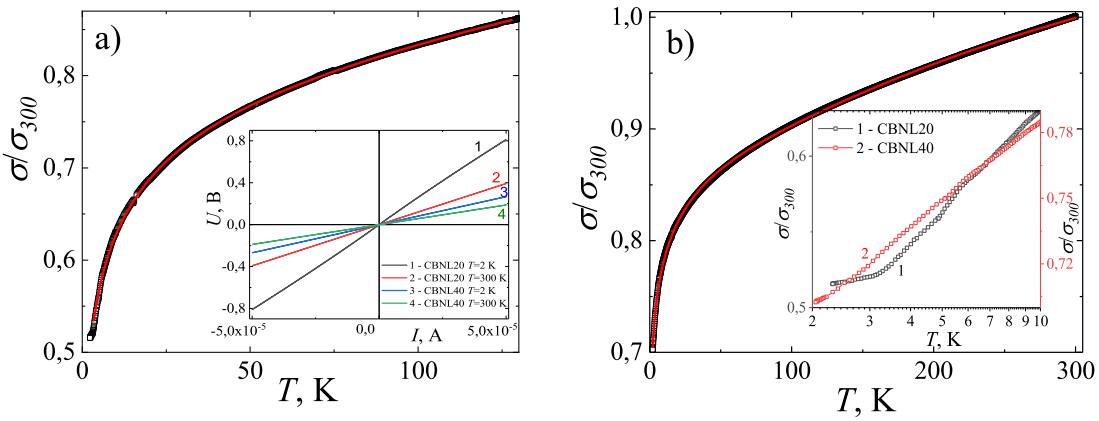

The inset to (a) show the I-Vs of samples $CBNL20$ (1, 2) and $CBNL40$ (3, 4), measured at temperatures of 2 K (1,3) and 300 K (2,4). The inset to (b) show temperature dependences of nomalized conductivity for the samples $CBNL20$ (black points 1) and $CBNL40$ (red points 2) in semilogarithmic scale.

Fig. 4. Temperature dependences of normalized conductivity $\sigma(T)/\sigma_{300}$ (where σ_{300} is conductivity at temperature T = 300 K) for samples *CBNL*20 (a) and *CBNL*40 (b). (For interpretation of the references to color in this figure legend, the reader is referred to the web version of this article.)

parameter α can be equal to 0.25 or 0.33 for 3*D* and 2*D* models of Mott *VRH*, respectively, or 0.5 and 0.33 in 3*D* and 2*D* samples accordingly for *VRH* Shklovskii–Efros model. Note that in the case of standard band model with constant activation energy $\alpha = 1$.

Another possible mechanism for the formation of low-temperature conductivity in *CBNL* may be the interference mechanism of quantum corrections (QC) to the Drude conductivity under conditions of weak localization [46]:

$$\sigma(T) = A + B \cdot \ln(T), \tag{2}$$

for the 2*D* case and

$$\sigma(T) = C + D \cdot \sqrt{T}, \tag{3}$$

for the 3*D* case, where A, B, C and D are model constants.

As we have shown by modeling, in its pure form, none of the mechanisms mentioned above describes experimental conductivity curves simultaneously over the entire temperature range (see Supplemental Material B). However, simultaneous consideration of both 2*D* and 3*D* QCs and the activation mechanism

$$\sigma(T) = A + B \cdot \ln(T) + D \cdot \sqrt{T} + E \cdot e^{-\triangle E/T}, \tag{4}$$

gives good agreement between the experimental and approximated conductivity curves (Fig. 4) over the entire temperature range. Here *A, B, D* are the constants as in relations (2) and (3) and $\triangle E$ – activation energy in semiconducting *CBNL* sublayer. The second term in relation (4) is responsible for 2*D* quantum corrections to Drude conductivity, the third term is for 3*D* ones, and the fourth term is for the band-like semiconducting (activational) mechanism.

The modeling carried out based on relations (1)–(4) showed that in both samples there are 2*D* quantum corrections to conductivity that are dominant at low temperatures. Activation mechanism in relation (4) with $\triangle E/\kappa_B \approx 296$ K and ≈ 384 K (κ_B is Boltzmann constant) for samples *CBNL*20 and *CBNL*40, respectively, plays a significant role at relatively high temperatures close to room temperature. The mechanism of quantum corrections for the 3*D* case appears only in sample *CBNL*40.

For the 2*D* case of quantum corrections theory, the following relationship is known for the temperature dependence of conductivity [58–60]:

$$\triangle\sigma = \beta\left(\frac{2e^2}{\pi^2\hbar}\right)\ln(T); \triangle\sigma \sim p\left(\frac{e^2}{\pi h}\right)\ln(T), \tag{5}$$

where e is the electron charge, $\hbar = h/2\pi$, h is Planck's constant, $\pi = 3.14$, β and p are the parameters responsible for the relationship between the phase breaking time and temperature and is in the range from 0.25 to 0.5 for β [58] and 1 or 2 for p [60]. Parameter $\beta((2e^2)/(\pi^2\hbar))$ or $p((e^2)/(\pi h))$,being an analog of approximation constant B in relations (3) and (5), must be in the range from $\approx 1.23 \cdot 10^{-5}\ \Omega^{-1}$ to $\approx 2.46 \cdot 10^{-5}\ \Omega^{-1}$. For our samples, considering conductivity normalization, constant B is close to the values of $\approx 1.2 \cdot 10^{-5}\ \Omega^{-1}$. This fact confirms the correctness of the approximation results. The value of the parameter $p = 1$ corresponds to the mechanism of scattering by defects [60].

The inset in Fig. 4b, shows the temperature dependences of the conductivity of samples *CBNL*20 (black dots) and *CBNL*40 (red dots) on a semi-logarithmic scale $\sigma(T)/\sigma_0 - Lg(T)$, which shows the saturation of the $\sigma(T)/\sigma_{300}$ curve at low temperatures. This effect is probably due to the tendency of the mean free path of charge carriers to the grain sizes with decreasing temperature, which was observed in polycrystalline graphene sheets in [55].

3.3. Magnetoresistance in carbon-based nanolayers samples

To further confirm the influence of QC mechanisms on carrier transport in *CBNL* samples, we present in Fig. 5 below the magnetic field dependences of relative magnetoresistance $MR(B) = [R(B,T) - R(0,T)]/R(0,T)$, measured for two orientations of vector **B** relative to sample plane — normally to the substrate plane and current vector **I** (*out-plane orientation*) and along the plane substrate but normally to current vector **I** (*in-plane orientation*).

Sample *CBNL*20 for out-plane orientation of **B** behaves rather like single-layer graphene with two main contributions into *MR(B)*, including Lorentz effect (giving positive *MR*) and probably quantum corrections in weak localization conditions (with negative *MR*) (Fig. 5a). For in-plane orientation of **B** the sample *CBNL*20 is characterized by only negative contribution into *MR* (Fig. 5b).

As is seen in Fig. 5a, *MR(B)* curves at temperatures below 25 K for the sample *CBNL*20 with out-plane orientation demonstrates negative magnetoresistance (*NMR*) over the entire range of magnetic fields under study. At $T > 25$ K, in the high-field region, features of a positive magnetoresistive effect (*PMR*) appears. In the case of an in-plane orientation of the magnetic field (Fig. 5b), only *NMR* is observed, the value of which is more than 2 times less than for out-plane orientation.

As is seen in Fig. 5c, the *CBNL*40 sample demonstrates only the presence of *NMR* effect for the out-plane magnetic field orientation. At the same time, with a planar orientation of the magnetic field (Fig. 5d) in the temperature range below 10 K, the *PMR* effect is observed with a tendency to saturate in strong fields and gradually decrease with increasing temperature.

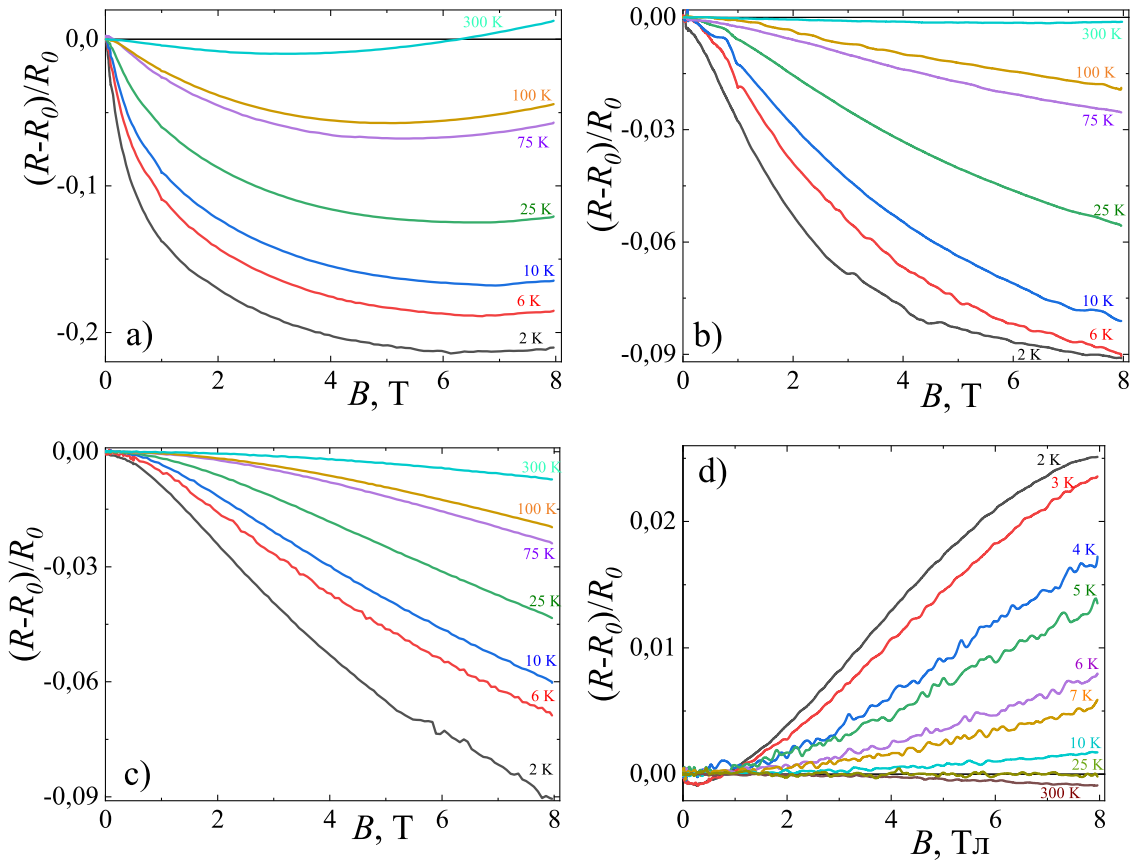

Fig. 5. Dependences of relative magnetoresistance $MR(B) = [R_{\square}(B,T) - R_{\square}(0,T)]/R_{\square}(0,T)$ for the sample *CBNL*20 *(a,b)* and *CBNL* 40 *(c,d)* with the orientation of the magnetic vector induction **B** out plane (*a,c*) and in plane (*b,d*) at different temperatures.

The *NMR* effect in the *CBNL*20 sample with out-plane orientation magnetic field (Fig. 5a) can be attributed to quantum corrections under WL conditions, which also manifested in $\sigma(T)$ curves described above. The appearance of the *PMR* is most likely due to the influence of the Lorentz mechanism on the movement of charge carriers. Note that an increase in the *NMR* is observed up to a magnetic field of 6 *T*, while, according to the theory [61], the *NMR* effect in such high magnetic fields should be absent. According to [45], the coexistence of 2*D* quantum corrections in the form of the *NMR* and the Lorentzian contribution in the form of the *PMR* in 2*D* or quasi-2*D* *CBNL*20 sample is possible only at out-plane orientation of a magnetic field. Because of this, for the in-plane orientation, the *PMR* effect is absent and a weakening of the *NMR* effect is observed (Fig. 5b).

Note that a comparison of the $MR(B)$ behavior in Fig. 6 for the perpendicular (out-plane) and longitudinal (in-plane) orientations of **B** vector demonstrates a significant difference in the region of relatively low fields. *MR(B)* curve 2 in Fig. 6 shows a faster *NMR* effect increase when growing of **B** with a perpendicular orientation compared to the longitudinal one (curve 1). Thus, the indicated features of the *NMR* effect for the *CBNL*20 sample are likely due to coexistence of, at least, two contributions: 2*D* quantum corrections (at *B* values lower than 0.01...0.02 T) and the *NMR* contribution (at *B* up to 6 T) due to any other mechanism, which is present both for longitudinal and perpendicular **B** orientations. We assume that this additional high-*B* contribution to the *NMR* effect may have the same abnormal nature as the anomalous magnetoresistance (*AMR*) effect, which was relatively recently discovered in some works. In papers [62–66], the *AMR* effect, approaching ~10% or more in some materials, was firstly observed in devices based on organic layers with non-magnetic electrodes and called the Organic *MR* effect (*OMAR*). Among the main features of the *AMR* effect, we can highlight the following:

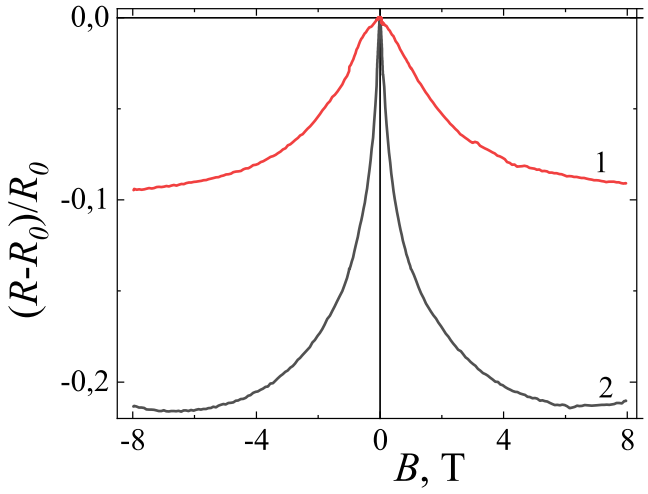

Fig. 6. Curves $MR(B) = [R_{\square}(B,T) - R_{\square}(0,T)]/R_{\square}(0,T)$ of the *CBNL*20 sample, measured with in-plane (1) and out-plane (2) orientation of magnetic field relative to the sample plane at temperature of 2 K.

- (a) *AMR* is the property of the layer bulk [62,63].
- (b) *AMR* is caused by hyperfine coupling [62,63,65].
- (c) *AMR* does not depend on the direction of the magnetic field [62,63,66].
- (d) *AMR*, depending on the material [62,63], obeys empirical laws like...

$$MR(B) \sim B^2/(|B| + B_0)^2, \quad (6)$$

or

$$MR(B) \sim B^2/(B^2 + B_0^2). \quad (7)$$

- (e) the *AMR* sign may be positive or negative, depending on the material and/or operating conditions of the devices [62,63,66].

At the moment, the *AMR* effect does not have an unambiguous description recognized by researchers. Most often, *AMR* is attributed to several mechanisms, which can be divided into two groups: hopping mechanisms of carrier transport and scattering by magnetic impurities.

In the case of the hopping mechanism, *AMR* is linked to the exponential asymptotic dependence of the electron bound state wave function on the distance from the donor (or acceptor) impurity [48] in a strong magnetic field. For a spherically symmetric Coulomb potential in a zero magnetic field, the wave function in a magnetic field becomes cigar-shaped, i.e., compressed in the direction transverse to the field [48,67]. This compression should lead to a significant reduction in the overlap of the tails of the electron wave functions on two neighboring donors, resulting in a substantial increase in resistance (*PMR*) under the influence of a magnetic field. Therefore, the exponential variation of *MR(B)* in the *PMR* region in sufficiently strong magnetic fields is considered as indication of hopping carrier transport. Conversely, in some hopping systems, such as amorphous germanium and silicon, an anomalous Negative Magnetoresistance contribution to *MR(B)* is observed. This is often attributed to the presence of frozen spins on some localized states [68]. The latter introduces into *MR(B)* dependence either the influence of charge carriers scattering with a spin flip or the influence of an increase in the density of localized states due to the Zeeman energy splitting $\sim\mu_B B$ [69]. This type of *NMR* manifests itself as a relatively small effect (<1%) even in relatively strong magnetic fields with $B \sim 1$ T [63,70].

Fukuyama and Yoshida [71] proposed a mechanism of electronic conduction due to variable range hopping (*VRH*) resulting from strong Anderson localization, i.e., without the participation of spins. This leads to a large *NMR* effect, especially near the metal-nonmetal transition, due to the exponential dependence of the rate of electron hopping by occupied energy levels (localized centers) on distance. This mechanism also manifests itself in the form of a strong dependence of conductivity on the electric field. The application of a magnetic field removes the degeneracy (splits) of energy states (Zeeman effect), resulting in the preferential population of energy levels in a higher Zeeman state. The wave function corresponding to these states has a large spatial extent, and the conductivity in a magnetic field is given by the relation:

$$\sigma(B) = \sigma_0 cosh(\alpha B), \quad (8)$$

where σ is conductivity in the field B, σ_0 – conductivity in $B = 0$, *cosh* – hyperbolic cosine. Coefficient α in (8) is

$$\alpha = \frac{\beta d}{n}\frac{g\mu_B}{2(E_C - E_F)}\left(\frac{T_0}{T}\right)^{\frac{1}{n}}, \quad (9)$$

where T_0 is characteristic temperature, depending on temperature, $n = 0.25$ according to Mott *VRH* mode and $n = 0.5$ for Shklovskii–Efros *VRH* regime.

Altshuler, Aronov and Khmelnitsky [32,72] showed that *NMR* can be caused by *VRH* jumps of coherent electrons (the same ones that are responsible for quantum corrections) by weakly localized states, taking into account the shift of the metal–insulator transition point in an external magnetic field. In [72], the dependence of resistance on the magnetic field is given by the relation

$$\ln\left(\frac{\rho(T,B)}{\rho(T,0)}\right) = \left(-A\nu\frac{1-\alpha}{\alpha}\right)\left(\frac{eB}{\hbar c}n^{-\frac{2}{3}}\right)^{\frac{1}{2\upsilon}}\ln\left(\frac{\rho(T)}{\rho_0}\right), \quad (10)$$

where constant $A \sim 1$, $\nu \approx 1/2$ [73] and n – concentration of carriers.

Alexandrov, Dediu and Kabanov [70] proposed a model of hopping magnetotransport depending on the sign of non-zero states of the orbital magnetic moment m. In this case, the course of $MR(B) \sim B$ for any non-zero magnetic quantum number (m) for the localized state. The value of m can be quite large if the bound state is small enough and/or the jump length is large enough. *MR(B)* is positive (*PMR*) for positive m and negative (*NMR*) for negative m. The unusual expansion of the wave function with a positive value of m is associated with a linear decrease in the ionization energy in weak magnetic fields due to influence the orbital magnetic moment. On the contrary, states with negative m are compressed, in particular, because of increasing their ionization energy with increasing magnetic field. As a result, the total change in conductivity with increasing magnetic field is given as the sum of the linear component (σ_m) and the exponential contribution (σ_s) due to the classical compression of the wave function [48]:

$$\sigma(B) = \sigma_m(B) + \sigma_s(B) = \sigma_{m0}\left(1 + \frac{B}{B_m}\right) + \sigma_{s0}e^{-\left(\frac{B}{B_s}\right)^2}, \quad (11)$$

where σ_{m0}, σ_{s0} are corresponding contributions in conductivities in $B = 0$; B_m, B_s – corresponding characteristic fields.

Additionally, *NMR* mechanisms based on hopping conduction include effects that arise in the presence of polarons. Initially, polaron models were developed for perovskite manganites [74–76]. Bobbert et al. modified the model for organic materials [63]. They assumed that conduction in disordered organic materials occurs due to hopping of charge carriers between localized sites, but due to the strong electron–ion interaction, electrons drifts in an electric field being surrounded by a cloud of positive charges of lattice ions (polarons). The mechanism is based on polaron hopping and the formation of bipolarons (a doubly occupied site) under the influence of random hyperfine fields of hydrogen-like impurities and an external magnetic field. Depending on the ratio of the rates of transitions from one site to another one with and without the formation of a bipolaron, two different shapes of *MR(B)* curves of type (6) and (7) are experimentally observed.

An alternative to the hopping-based models was developed in [77–80] where *NMR* effect was attributed to the spin-dependent scattering of charge carriers by localized magnetic moments of paramagnetic centers. The application of an external magnetic field orders these magnetic moments (and the faster the lower temperature), which suppresses carrier scattering and, accordingly, increases conductivity [77–79]. As a result, the *NMR* effect is described by the relations:

$$\frac{\Delta\rho}{\rho_0} = -\left(C \cdot L\left(\frac{\mu^* B}{k_B(T+\Theta)}\right)\right)^2, \quad (12)$$

or

$$\frac{\Delta\rho}{\rho_0} = -C \cdot L\left(\frac{\mu^* B}{k_B(T+\Theta)}\right), \quad (13)$$

where

$$L\left(\frac{\mu^* B}{k_B(T+\Theta)}\right) = \coth\left(\frac{\mu^* B}{k_B(T+\Theta)}\right) - \frac{k_B(T+\Theta)}{\mu^* B},$$

is Langevin function; ρ – resistivity of the sample in non-zero B; ρ_0 – resistivity of the sample in $B = 0$; Θ – Qurie temperature, μ^* - magnetic moments of scattering centers.

At $\Theta = 0$ Eqs. (12) and (13) are transformed in relations

$$\frac{\Delta\rho}{\rho_0} = -\left(C \cdot L\left(\frac{\mu^* B}{k_B T}\right)\right)^2, \quad (14)$$

$$\frac{\Delta\rho}{\rho_0} = -C \cdot L\left(\frac{\mu^* B}{k_B T}\right). \quad (15)$$

Close behavior is observed at electron–magnon scattering, since the density of spin waves increases with increasing temperature. This effect was described by [81] on the base of expression

$$\Delta\rho_{xx}(T,B) \propto \frac{BT}{D(T)^2}\ln\left(\frac{\mu_B B}{k_B T}\right), \quad (16)$$

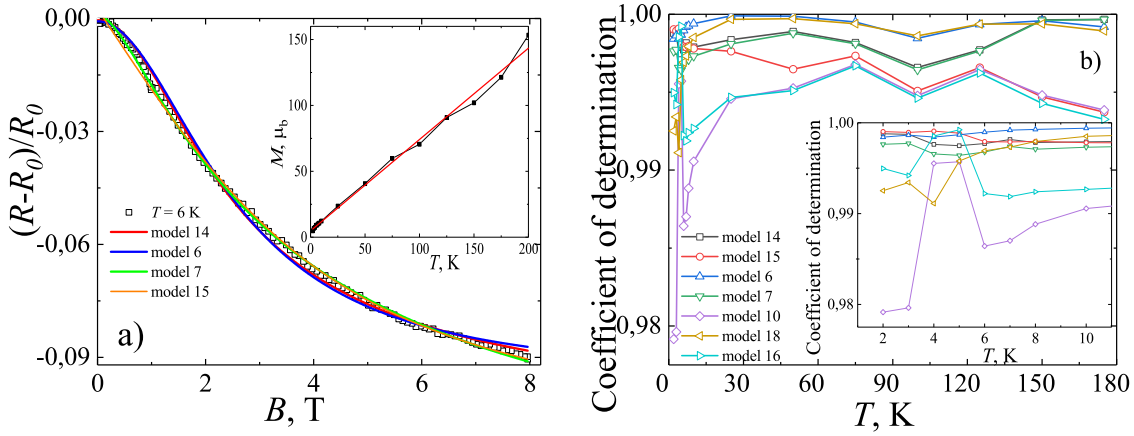

The inset in figure (a) shows the dependence of the magnetic moment of the paramagnetic scattering centers in Bohr magnetons on temperature, calculated from the *MR(B)* curves for the *CBNL*20 sample using model (14).

Fig. 7. (a) Dependence of the relative magnetoresistance $MR(B) = [R_{\square}(B,T) - R_{\square}(0,T)]/R_{\square}(0,T)$ on magnetic induction for the *CBNL*20 sample measured at T = 6 K (points) and its approximation by models (6), (7), (14) and (15). (b) Determination coefficient (R^2) for approximations of the *MR(B)* dependences for the *CBNL*20 sample by models (6), (7), (10), (14)–(16) and (18) in the temperature range 2...300 K. The magnetic field orientation is parallel to the sample plane.

which is valid at intermediate temperatures. Here $D(T)$ is the magnon stiffness or magnon renormalization mass, ν_B is the Bohr magneton and k_B is the Boltzmann constant. It is seen that magnon contribution to magnetoresistive effect can be both positive (at $\mu_B B \geq k_B T$) and negative ($\mu_B B \leq k_B T$).

Under conditions of weak localization, the *NMR* effect can be described by the Aronov–Altshuler theory for interference quantum corrections [82] to Drude sheet conductivity in form:

$$\Delta\sigma_{\square} = \frac{e^2}{\pi h} F\left(\frac{B}{B_{\phi}}\right), \tag{17}$$

or [61]

$$\Delta R_{\square} = -\frac{e^2\rho^2}{\pi h} F\left(\frac{B}{B_{\phi}}\right), \tag{18}$$

where

$$F(x) = \ln(x) + \psi\left(0.5 + x^{-1}\right), \tag{19}$$

ψ is digamma function. Here the parameter $x = B/B_{\varphi}$ is determined by the ratio of the induction of the external magnetic field B to a certain characteristic field B_{φ}. The characteristic field B_{φ} describes scattering processes without phase breaking of wave function. It determines the phase breaking times

$$\tau_{\phi} = \frac{\hbar c}{4eD} B_{\varphi}^{-1}, \tag{20}$$

during elastic or quasi-elastic scattering of charge carriers. Here D is diffusion coefficient for electrons.

Within the framework of the above-described models, identifying the nature of the *NMR* component, which for sample *CBNL*20 is present both for longitudinal and perpendicular orientations of the magnetic field, is easier to carry out for the longitudinal orientation of the magnetic field, because the influence of 2*D* quantum corrections and the Lorentz mechanism on the behavior of the *MR(B)* curves can be ignored. An example of approximation of experimental *MR(B)* curves with the above-described models at T = 6 K is shown in Fig. 7a (the complete approximation procedure under all considered temperatures and for all models mentioned above is given in Supplemental Material C).

Fig. 7b shows the coefficient of determination (R^2) for approximations of the magnetic field dependences of *MR(B)* for the *CBNL*20 sample by models (6), (7), (10), (14)–(16) and (18). Analysis of models (8) and (11) was not carried out on this graph since, on the one hand, these models were tested for magnetoconductivity $MC(B) = [\sigma_{\square}(B,T) - \sigma_{\square}(0,T)]/\sigma_{\square}(0,T)$, and on the other hand, as can be seen from Supplemental Material C (Figure C.4) these models cannot describe the experimental data. To a rough approximation, models (6), (7), (10), (14)–(16) and (18) adequately describe the experimental data. However, as can be seen in Fig. 7b, the worst agreement over the entire temperature range is shown by models (10) and (16). In the region of relatively high temperatures (>25 K), good agreement is shown by model (18) characteristic of quantum corrections, however, model (18), on the one hand, shows poor agreement at temperatures below T = 25 K, and on the other hand, as noted above, their presence seems unlikely due to the small thickness of the sample.

The remaining models can be divided into two groups: (*i*) models (6) and (7) characteristic of *AMR* [63] and (*ii*) models (14) and (15) and those given in [77–79], associated with scattering by magnetic impurities. Calculations have showed that model (6) has an advantage over model (7), and (14) over (15). It is worth noting that models (6) and (14) describe the behavior of relative magnetoconductivity *MC(B)* in low magnetic fields much better than the other models under consideration, which also indicate the priority of models (6) and (14) over others. In this case, we observe a slightly better approximation of the *MR(B)* dependences we obtained by model (6) compared to other mechanisms, which may indicate the possibility of the formation of bipolarons, and *MR(B)* is better described by the model proposed in [63]. However, as described above, analysis of the temperature dependence of conductivity indicates that there is no significant contribution from hopping conductivity at temperatures below 50 K (according to modeling, it does not exceed 0.03% and decreases exponentially with decreasing temperature). Therefore, it seems unlikely that the contribution from the hopping mechanism to the total magnetoresistance *MR(B)*, at low temperatures, will have a value of about 9%. Otherwise, this would mean that the contribution of the hopping component $MR_{hop}(B)$ to the total *MR(B)* is ≈13000% at T = 50 K and increases exponentially when temperature decreasing. Based on the above, in our opinion, the most probable of the listed models is model (14) associated with taking into account spin-dependent scattering during the charge carrier transport, which will be explained below.

Taking into account the above described, it seems more likely that the mechanism of scattering of electrons by localized magnetic moments M caused by the presence of spins on paramagnetic defects and dopant impurities (see, for example, work [83] for semiconductor materials), rather than doping them with magnetic ions. In carbon-based materials and structures, the formation of spin subsystem on paramagnetic centers (i.e., even in the absence of magnetic ions in

the samples) was predicted theoretically in [84–89] and discovered experimentally in [90–97] as observation of magnetization moment M due to ferromagnetic ordering of spins on paramagnetic centers. In particular, open-loop ferromagnetism was observed in highly oriented pyrolytic graphite (HOPG) at 5 and 300 K, which was attributed to localized electron states at the grain boundaries of HOPG, forming two-dimensional arrays of point defects [93]. In pyrolytic carbon, positive magnetization was recorded up to 800 K [98]. In graphene, super-paramagnetism was observed at room temperature based on graphene quantum dots [95]. The example of our assessment of the $M(T)$ curve from the $MR(B)$ dependences using relation (14) is presented in the inset of Fig. 7a. The observed linear dependence $M(T) \sim T$ with increasing temperature seems unusual, since it would be more logical to either remain constant (as, for example, in a ferromagnet below the Curie temperature) or decrease the $M(T)$ with increasing temperature (due to spin disordering by lattice ions vibration). However, the same linear increase of $M(T)$ in pyrolytic carbon, as well as in hydrogenated multilayer graphene has been reported in the literature [98,99].

Let us consider the possible nature of the occurrence of such a magnetic moment, which increases with temperature growth. One of the possible mechanism for the occurrence of local magnetic inclusions due to, for example, the formation of a magnetic polarons, was described in [99]. As shown above, sample *CBNL*20 has an activation component of conductivity. Due to the strong electron–ion interaction, electrons drift in an electric field being surrounded by a cloud of positive charges of lattice ions with their spins, that just means the emergence of a magnetic polaron. When the magnetic moments in this cloud become oriented under the influence of a magnetic field, the polaron can be considered as a kind of particle with a relatively large magnetic moment. The increase in the magnetic moment with increasing temperature can be associated with the overlap of several neighboring magnetic sections (magnetic polarons) into one system. Additional possible mechanism for the formation of magnetic ordering can be the indirect RKKY (Ruderman–Kittel–Kasuya–Yoshida) exchange interaction between paramagnetic ions, carried out through intrinsic conduction electrons. The presence activation component of conductivity in *CBNL* samples can lead to an increase in the number of conduction electrons with increasing temperature, which can enhance the RKKY exchange interaction and, as a consequence, the growth of magnetic moment with temperature. It is also worth mentioning that an increase in magnetization with increasing temperature is possible in Neels theory of ferrimagnetism [100,101].

The mentioned above means that the appearance in the carbon-based structure of inhomogeneities (inclusions) with a strong ferromagnetic spin interaction leads to a number of important consequences. In particular, when a perpendicular magnetic field is applied to the *CBNL*20 sample plane, there are most likely two components of *NMR* effect: due to QCs (for WL conditions) in low (not higher than 0.5 T) magnetic fields and of the mechanisms of electron scattering by localized magnetic moments in B up to 8 T. To these contributions, the *PMR* effect is added as a result of the influence of the Lorentz force on the drift of charge carriers. With this approach, the behavior of conductivity in perpendicular a magnetic field can be described as a sum of the indicated mechanisms:

$$\sigma = \sigma_{\mathrm{WL}} + \sigma_{\mathrm{M}} + \sigma_{\mathrm{Lor}}, \tag{21}$$

where σ_{WL} is quantum corrections contribution described by model (17), σ_{M} – contribution due to electron scattering by localized magnetic moments (model (14)), and σ_{Lor} – Lorentz-like contribution (model (23)). As a result, the formulae (21) can be transformed to the relation:

$$\sigma(B) = \sigma_0 + \frac{e^2}{\pi\hbar}\left[\ln\left(\frac{B}{B_\phi}\right) + \psi\left(\frac{1}{2} + \frac{B_\phi}{B}\right)\right] + \frac{\sigma_{M0}}{1 - \left(C \cdot \left(\coth\left(\frac{\mu^* B}{k_B T}\right) - \frac{k_B T}{\mu^* B}\right)\right)^2} + \frac{\sigma_{Lor0}}{1 + \mu^2 B^2}, \tag{22}$$

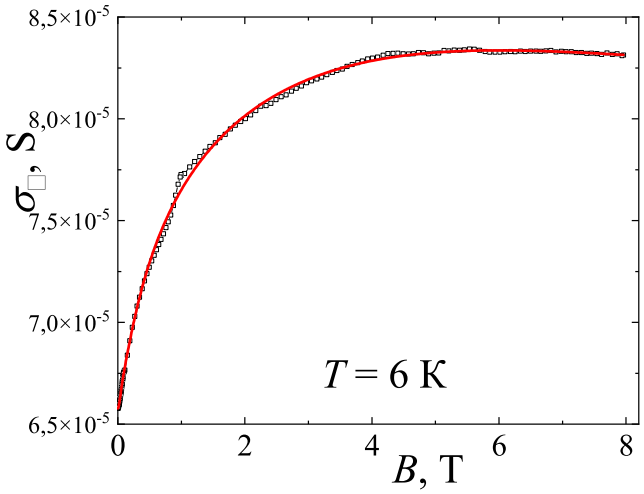

Fig. 8. Dependence of sheet conductivity $\sigma_{\square}(B)$ of the *CBNL*20 sample on the magnetic induction (curve with black dots) and its approximation by formula (22) (red curve) for T = 6 K. The magnetic field orientation is normal to the sample plane.

where σ_0, σ_{M0}, σ_{Lor} are related contributions to conductivities in $B = 0$. Note that the second term in the relation (21) is the value of quantum correction in $B \neq 0$.

Fig. 8 shows, as an example, the experimental curve of sheet conductivity versus magnetic field $\sigma(B)$ at a temperature of 6 K for a perpendicular orientation of the magnetic field relative to the plane of the *CBNL*20 sample and its approximation by relation (22). This behavior of the $\sigma(B)$ curves turned out to be characteristic for all temperatures studied and takes into account contributions from the quantum corrections, scattering by magnetic-like centers and the Lorentz mechanism of *MR(B)*. The fitting parameters values estimated from model (22) gave a rather wide set of physically acceptable values with close errors. For example, the range of acceptable values of charge carrier mobility and characteristic field of phase breaking was in the range $\mu = 0.1 \pm 0.1$ m^2/(Vs) and $B_\varphi = 0.02 \pm 0.01$ T respectively. Such a scatter of the sought fitting parameters does not allow us to give an unambiguous conclusion about the nature of the processes occurring in the sample both when the magnetic field and temperature change. Nevertheless, the very fact of the presence of magnetic inhomogeneities (inclusions) and their influence on the dependences $\sigma(B,T)$ can be considered proven.

As described earlier, when a magnetic field is applied along the *CBNL*40 sample at temperatures below 10 K, a *PMR* effect is observed (Fig. 5d) with features characteristic of the Lorentzian mechanism. The absence of the *NMR* effect in this sample with in-plane (**B**) orientation most likely indicates the disappearance or strong weakening of the *MR(B)* contribution due to spin-dependent scattering of charge carriers, which was characteristic of the *CBNL*20 sample. Possible reasons for the disappearance of this mechanism will be discussed below.

Let us recall that, as earlier presented when analyzing the temperature dependences of conductivity, the *CBNL*40 sample shows not only 2*D*, but also 3*D* behavior of quantum corrections to the Drude conductivity. The latter indicates a transition from the quasi-2*D* behavior of the thinner *CBNL*20 sample (≈20 nm thick) to the mixed 2*D*/3*D* behavior for the *CBNL*40 sample with a thickness of ≈35 nm. Manifestations of the Lorentzian-like *PMR* contribution to the *MR(B)*:

$$MR(B) = \mu^2 B^2, \tag{23}$$

measured along the plane of the sample, allows one to estimate the mobility of charge carriers μ [37,102]. Examples of experimental and approximation curves *MR(B)* at T = 2 K and $\mu(T)$ at $2 < T < 10$ K for

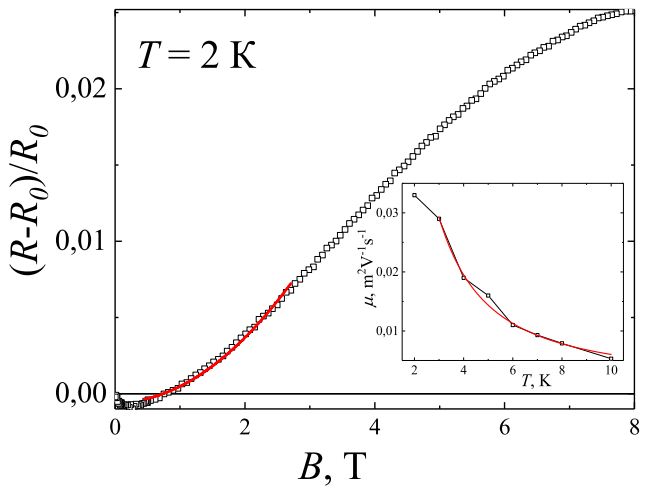

The inset shows the temperature dependences of charge carrier mobility μ (black dots) and its approximation by equation (24) (red curve).

Fig. 9. Dependence of the relative magnetoresistance $MR(B) = [R_{\square}(B,T) - R_{\square}(0,T)]/R_{\square}(0,T)$ on magnetic induction for the *CBNL*40 sample measured at T = 2 K (points) and its approximation by model (23) (red curve). The magnetic field orientation is parallel to the sample plane.

the sample *CBNL*40 with in-plane **B** orientation are shown in Fig. 9 . Approximations of *MR(B)* at all temperatures in the range from 2...10 K are given in Supplemental Material C. As can be seen from the solid red curve in Fig. 9 (inset), in the temperature range 2...10 K the dependence $\mu(T)$ is well described by the relation

$$\mu = \frac{4e\ell\tau_0}{3\sqrt{\pi}(m^*)^{0.5}k_b^{0.5}}T^{-\frac{3}{2}}, \tag{24}$$

which, according to [37] corresponds to the scattering of carriers by phonons, however, this requires additional evidence due to the peculiarities of conductivity for interplane motion in graphite. Here m^* is the effective mass of the electrons, l is the mean free path of the conduction electron, τ_0 is the relaxation time. The deviation of $\mu(T)$ from relation (24) at T < 3 K correlates with the tendency for the $\sigma(T)/\sigma_0$ curve to reach saturation on a semi-logarithmic scale ($\sigma(T)/\sigma_0$–Lg(T)) at the same temperature in the inset to Fig. 4b above. As noted earlier, this effect is most likely due to the fact that in polycrystalline samples the ℓ value tends to the size of the conducting grains when temperature decreases [55,82], so that the mobility ceases to depend on temperature.

The behavior of the $MR(B)$ curves for out-plane orientation of the magnetic field for the *CBNL*40 sample also differs significantly from the behavior of those for the *CBNL*20 sample. This, in particular, is manifested by the lack of a noticeable contribution of *PMR* to magnetoresistance and the shift of *MR(B)* curves, where *NMR* is observed, to the region of stronger magnetic fields. Fig. 10a, shows the corresponding approximations of the experimental curves *MR(B)* by the above-described models at T = 6 K (the approximation for all temperatures and at all models is given in Supplemental Material C, Figure C.7...C.9. Corresponding coefficients of determination (R^2) for approximating the $MR(B)$ in the temperature range 2...300 K for sample *CBNL*40 are given in Fig. 10b.

At the same time, it should be noted that almost all of the mentioned models are, to a rough approximation, capable of describing experimental curves, but in different temperature ranges. For example, models (15) and (16) describe the behavior of $MR(B)$ relatively well at low temperatures, but poorly describe them at high temperatures. Other models (e.g. (7), (8), (10), (11) and (14)), on the contrary, correspond to better R^2 values at higher temperatures.

Over the entire temperature range studied, the experimental $MR(B)$ curves are described better by models (6) and (18), as can be seen from Fig. 10. However, the values of the parameter B_{φ}, extracted from relation (18) and presented in the inset to Fig. 10a, when approximating $MR(B)$ curves for the *CBNL*40 sample, turned out to be noticeably higher than those usually given in the literature for carbon materials. To explain the nature of the overestimation of the B_{φ} and other unusual features of the behavior of the studied *CBNL* samples, a phenomenological model is presented below that links the $MR(B)$ and $MC(B)$ curves to their structure.

3.4. Phenomenological model for explanation of MR (B) and MC(B) behavior in carbon-based nanolayers

Our study of the temperature and magnetic field dependences of conductivity allows us to describe phenomenologically the main changes in charge carrier transport features in *CBNL* structures with the evolution of their morphology and atomic structure.

As noted above, *SEM* images of samples deposited for 20 and 40 min showed the absence of developed percolation structures characteristic of vertical graphene (*VG*). As a result, the surface of samples *CBNL*20 and *CBNL*40 has a fairly uniform structure with the presence of a large number of unconnected island-nuclei of the future *VG* phase, close to elliptical in shape, which nucleate on the surface of a continuous nanographite sublayer (see, Fig. 1). It can be seen that increasing the growth time to 40 min leads to both an increase in the thickness of the nanographite sublayer from ≈20 nm (*CBNL*20, Fig. 2a) to ≈35 nm (*CBNL*40, Fig. 2b), and to an increase in the size of elongated ellipsoidal nuclei. At the same time, as it turned out, the concentration of islands (nuclei of *VG* phase) decreased approximately 5 times from $2.5 \cdot 10^{10}$ cm^{-2} to $5.4 \cdot 10^{9}$ cm^{-2} for samples *CBNL*20 and *CBNL*40, accordingly.

Let us remind the known from the literature model of the nucleation and growth of the *VG* phase with increasing time of *PECVD* synthesis of *CBNL*. As noted earlier in [53], initially, when CH_4 is inserted into the reactor, various free carbon and hydro-carbon species are generated via CH_4 easy conversion to CH_x (x = 1...3) radicals through radicals' recombination due to C_2 dimers production and subsequent dissociation. The reactive carbon dimers (C_2) are believed to play an important role especially for the formation of critical nuclei and later growth of *VG* phase. These active species are adsorbed onto energetically most favorable regions on the substrate starting the nucleation of nanographitic (NG) domains. As these domains grow, they coalesce and form particularly defective continuous interfacial nanographitic base layer containing a-C, carbon onions, pentagon- and heptagon-like rings, and other defects. Then secondary nucleation starts and hereafter the growth of vertically aligned graphene flake-like nanostructures generally at the defected sites of the *NG* base layer. During the synthesis, H atoms simultaneously act as an effective etchant rapidly removing undesirable amorphous phases, weaker sp^3 hybridized carbon bonds, and equally extracting bonding atoms from the gas-phase radicals, promoting the crystalline graphitic structure and the sharp edges in the layers. Adsorbed carbon atoms form strong C–C covalent bonds at the edges of *VG* phase and weak van der Waals bonds between graphite layers, which are constantly bombarded by atomic H.

At the same time, it is shown in [103] that during the synthesis of *VG* in a buffer nanographite sublayer, a thin layer can be formed consisting of substrate and carbon atoms mixed together, which leads to matching the lattice parameters of the substrate and the nanographite sublayer [103,104]. After this, according to [53,103,104], graphite layers grow parallel to the surface of the substrate, and defects on which the *VG* phase nucleates appear during the deposition process due to the effects of the sprayed gas [103] (Fig. 11c). Thus, taking into account the schematic images of the *VG* phase growth, previously given in works [103,104], the structure of samples *CBNL*20 and *CBNL*40 can

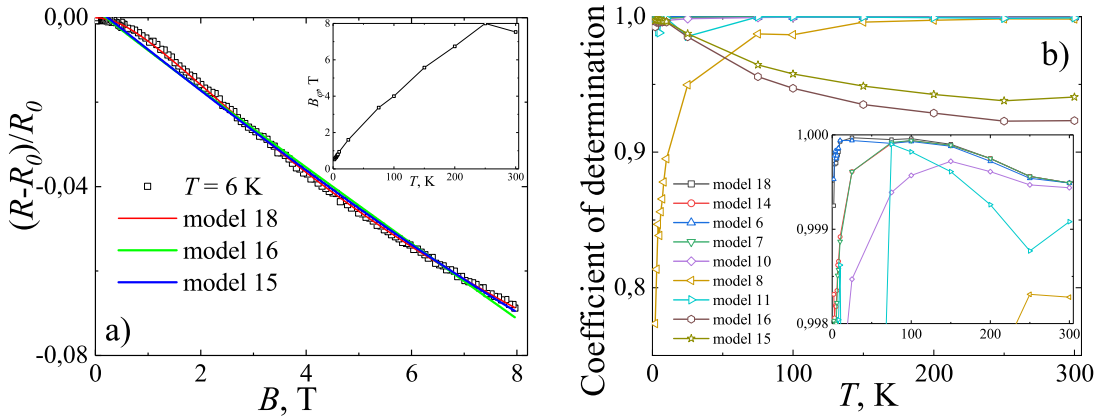

The inset in (a) shows the dependence of the parameter B_φ on the temperature, extracted from the model approximation (18).

Fig. 10. (a) Dependences of the relative magnetoresistance $MR(B) = [R_\square(B,T) - R_\square(0,T)]/R_\square(0,T)$ of the *CBNL*40 sample measured at $T = 6$ K (points) and its approximations by models (14), (15) and (17). (b) Determination coefficient (R^2) when approximating the magnetic field dependences $MR(B)$ and $MC(B)$ of the *CBNL*40 sample with models (6), (7), (10), (14), (15), (16) and (18) in the temperature range 2...300 K. The magnetic field orientation is normal to the sample plane.

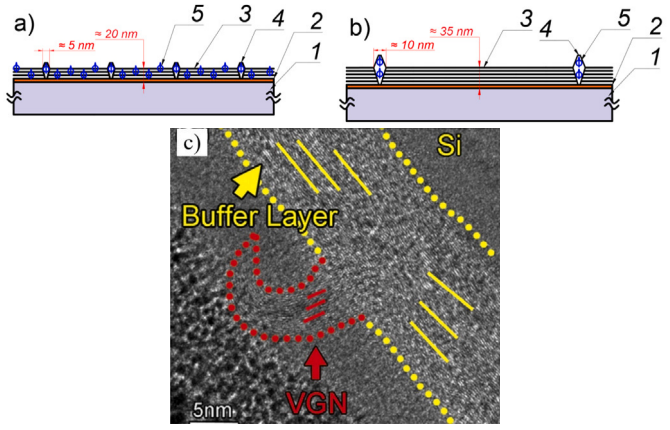

1 – substrate, 2 – buffer layer,
3 – nanographite sublayer, 4 – *VG* phase nuclei,
5 – paramagnetic defects in the nanographite sublayer.

Fig. 11. Schematic representation of the structure of *CBNL*20 (a) and *CBNL*40 (b) samples in cross section and (c) – TEM of the interface between the *VG* and the Si substrate [103].

be represented as shown in Fig. 11. At the first stages (short times) of deposition, a thin buffer layer 2 is formed on the substrate 1, consisting of substrate and carbon atoms mixed together. A nanographite sublayer 3 is formed on this layer, which is the main conducting agent in our experiment. On defects in the nanographite sublayer (most likely these are the boundaries of nanographite crystallites), the *VG* phase nuclei are formed 4. It should be noted that in the nanographite sublayer of sample *CBNL*20 in Fig. 11a, a large number of point defects appear between small ellipse-like nuclei of future *VG* phase 5. The latter act as paramagnetic centers on which spin-dependent scattering of charge carriers occurs. After this, with an increase in the synthesis time (i.e., when the *CBNL*40 sample is grown), a part of these point defects between the nucleating islands disappear under the influence of H atoms, but most likely remain either inside the *VG* phase or at the *VG* phase/*CBNL* interfaces. Let us recall that the concentration of the *VG* phase in this sample decreases by approximately 5 times. Therefore, the upper part of the nanographite sublayer 3 in the *CBNL*40 sample (see region 3 in Fig. 11b), formed at times exceeding 20 min between *VG* phase islands, has a more perfect crystal structure, which ensures an increase in the observed conductivity.

Based on the structural model shown in Fig. 11, it is possible to formulate a phenomenological model linking the observed effects of carrier transport with the proposed description of the structure of the samples. This model is drown up in Figs. 12 and 13 (for *CBNL*20 and *CBNL*40 respectively) in form of some schematic diagrams of the charge carrier drift (in form of current trajectories) along the graphite sublayer in zero magnetic field (Fig. 12a and b and 13a and b) and in magnetic fields with in-plane (Fig. 12c and d and 13c and d) and out-plane (Fig. 12e and f and 13e and f) orientation relative to the sample plane.

As noted earlier, in the *CBNL*20 sample two main mechanisms are responsible for the temperature dependence of conductivity $\sigma(T)$: two-dimensional quantum corrections that describe the interference contribution to the Drude conductivity under conditions of weak localization, and the activation mechanism, which makes a noticeable contribution only at relatively higher temperatures (150...300 K). Magnetotransport of charge carriers in *CBNL*20 depends on the orientation of the magnetic field relative to the sample plane. Thus, with a perpendicular (out-plane) orientation of the magnetic field in this sample, three contributions to the magnetoresistance (*MR*) are observed: from a two-dimensional quantum correction (I), from scattering on (para)magnetic defects (II) and due to the Lorentz mechanism (III). With the longitudinal (in-plane) orientation of vector **B**, the quantum correction and the Lorentz mechanism of $MR(B)$ does not appear in the *CBNL*20 sample due to the impossibility of deflecting charge carriers under the influence of Lorentz force in out-plane oriented **B** vector relative to the sample plane due to the small thickness of the latter. At the same time, the mechanism (II) of scattering on the spins of paramagnetic defects manifests itself in the form of *NMR* effect observation.

According to this model, the movement of carriers from one electrical contact to another current lines J along nanographite sublayer 2 under the influence of an electric field in *CBNL*20 sample in zero magnetic field (Fig. 12a and b) are controlled by trajectories consisting of three types of images. Trajectory sections of type 4 (Fig. 12b) correspond to the diffusion of charge carriers along circular (or self-intersecting) trajectories, which is described by the Aronov–Altshuler theory of quantum corrections in weak localization (WL) conditions. Sections of current lines of type 7 symbolize the enveloping of current trajectories J around the most defective areas (type 3) of the graphite sublayer under *VG* phase islands with strong magnetic moments (Fig. 12b). Sections of current lines in the vicinity of centers of type 6 symbolize the interaction of electrons with chaotically located single paramagnetic centers 6 (Fig. 12a and b).

When the sample *CBNL*20 is introduced into a longitudinal magnetic field (Fig. 12c and d) the trajectories of type 4 from WL effects remain,

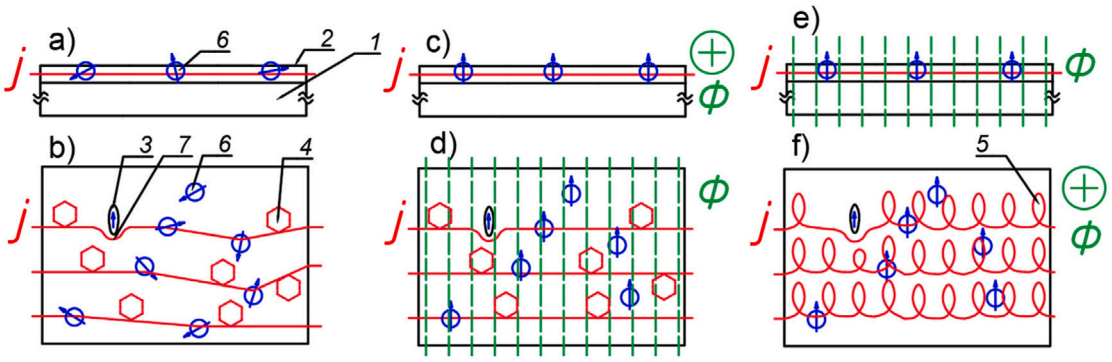

a, c, e – sectional view, b, d, f – top view;
1 – substrate, 2 – conducting nanographite sublayer, 3 – island-nuclei of the *VG* phase with clusters of paramagnetic centers (defects), 4 – self-intersecting trajectories of carriers, providing a contribution to the conductivity from the *WL* mechanism, 5 – Lorentz -like (cycloidal) trajectories of carriers in a magnetic field, 6 – (para)magnetic scattering centers, 7 – trajectories, enveloping islands of *VG* phase.
Magnetic flux Φ is indicated by green lines, current lines *J* are red lines, blue arrows indicate magnetic moments. To avoid overloading the pictures with symbolic images, only one ellipse-like island 3 is shown in them.

Fig. 12. Schematic representation of the transport of charge carriers in sample *CBNL*20 without a magnetic field (a,b) and in a magnetic field with in-plane (c,d) and out-plane (e,f) orientations of vector **B**. (For interpretation of the references to color in this figure legend, the reader is referred to the web version of this article.)

while scattering on type 6 paramagnetic centers should decrease due to the alignment of spins along the lines of magnetic flux Φ (it manifests itself in observations of *NMR* effect). Note that the shift of electrons normally to the plane of this sample under the influence of Lorentz force is impossible for this case due to small thickness of the sample, which leads to the absence of cycloidal sections of current lines in Fig. 12c. For out-plane orientation of the **B** vector (Fig. 12e and f), the WL effects are destroyed at $B < 200$ mT and self-crossing trajectories 4 must disappear (Fig. 12f), scattering on paramagnetic centers 6 is weakened (for both cases we observe the *PMR* effect). But the deflection of charge carriers under the influence of the Lorentz force appears in form cycloid-like parts 5 of trajectories in Fig. 12f with observation of *PMR* effect. Type 7 trajectories due to rounding of *VG* phase islands by *J* trajectories (Fig. 12f) will be discussed below.

Now discuss transport carrier in terms of the proposed phenomenological model for the case of *CBNL*40 sample that is presented in Fig. 13. Begin this discussion since noting the two most important features of magnetoresistivity (*MR*)/ magnetoconductivity (*MC*) dependences for the thicker nanographite sublayer 2. Firstly, the manifestation of mechanism (II), attributed above by us for *CBNL*20 sample to the scattering of charge carriers on the spins of single paramagnetic centers 6 in Fig. 12, which disappears in the *CBNL*40 sample. Secondly, for out-plane orientation of **B** vector, the *MR*(*B*) curves correspond to the WL model, but manifests itself in fields noticeably greater than those predicted by the Aronov–Altshuler theory. We interpret the reasons of these inconsistencies with the theory by the formation of local clusters of paramagnetic centers under island-like *VG*-phase region in the *CBNL*40 sample with strong ferromagnetic moments *M* which are capable of drawing in (introvert) magnetic flux. This inhomogeneous redistribution of magnetic flux Φ by the conductive carbon layer plane, presented schematically in Fig. 13e results in enhancing the magnetic field *B* over the *VG* phase islands (in the vicinity of these "magnetic" spin-enriched clusters with strong *M*) and weakening of *B* values between the nuclei islands of *VG* phase. As a result, these regions behave theirselves differently in electric sense than those in the *CBNL*20 sample.

To understand this case in more details, we recall that in *SEM* images formed by reflected electrons, islands are present in the form of contrasting light areas (Fig. 1). The white color of the latter against the background of dark gray areas of the nanographite sublayer may indicate the accumulation of charge on these *VG* phase islands. This, in turn, may indicate a weak electrical interaction between these spin-enriched clusters and the general conducting nanographite sublayer, which prevents charge drainage from them. The above allows us to attribute the bright island-like areas in the *SEM* images in Fig. 1 to those highlighted in Fig. 13 (type 3) by "magnetic" clusters isolated from the general electrically conductive layer. In our opinion, it is the more coarse island-like nuclei of the *VG* phase in the *CBNL*40 sample that are responsible for the retraction of the magnetic field, which is schematically depicted in Fig. 13e.

Therefore, summarizing the above mentioned, we can state that the described inhomogeneous distribution of the magnetic flux means that in the *CBNL*40 sample the islands and the parts of the nanographite sublayer between them are affected by magnetic fields of different magnitudes. This allows to give a consistent schematic explanation of carrier transport in *CBNL*40 sample as in zero magnetic field (Fig. 13a and b) and in a magnetic field lying parallel (Fig. 13c and d) and perpendicular (Fig. 13e and f) to the plane of the sample. Thus, the movement of charge carriers from one electrical contact to another in zero magnetic field (Fig. 13a and b) is described by the presence of self-crossing trajectories of type 4 due to WL effects (Fig. 13b). In this case, the current lines 7 bend around islands of the *VG* phase (Fig. 13b), which were possibly observed in the *CBNL*20 sample too (Fig. 12b). When the sample is under subjection of in-plane oriented magnetic field, the bending of current trajectories around *VG*-phase islands (type 7) and WL effects (type 4) are preserved (Fig. 13d), while in the region of low temperatures the *PMR* effect is observed due to the possibility of carriers moving perpendicular to the sample plane under the influence of Lorentz force (type 5 in Fig. 13c).

For out-plane orientation of the magnetic field (Fig. 13e and f), WL effects are suppressed (we observe *NMR* effect), and the bending of current trajectories 7 around the *VG* islands is persists. In addition note that in this case it becomes possible to deflect carriers under the influence of the Lorentz force (type 5 trajectories in Fig. 13f), which should lead to the observation of the *PMR* effect, however, in this experiment the *PMR* effect is not observed. Consequently, in the perpendicular magnetic field, the local redistribution of the magnetic flux Φ (Fig. 13e) manifests itself in the seeming displacement of the effect *NMR* from the WL contribution to the region of significantly larger fields and the lack of observation in our measurements of the *PMR* effect.

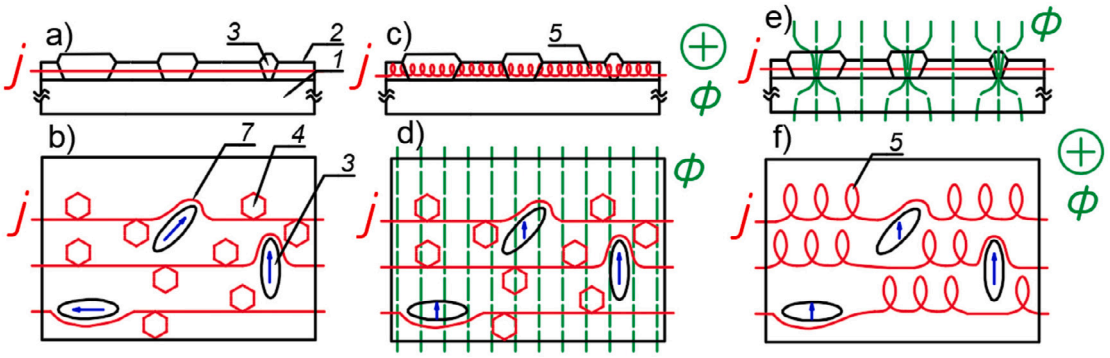

a, c, e – sectional view, b, d, f – top view;
1 – substrate, 2 – conducting nanographite sublayer, 3 – island-nuclei of the *VG* phase with clusters of paramagnetic centers (defects), 4 – self-intersecting trajectories of carriers, providing a contribution to the conductivity from the *WL* mechanism, 5 – Lorentz -like (cycloidal) trajectories of carriers in a magnetic field, 7 – trajectories, enveloping islands of *VG* phase.
Magnetic flux Φ is indicated by green lines, current lines *J* are red lines, blue arrows indicate magnetic moments.

Fig. 13. Schematic representation of the transport of charge carriers in sample *CBNL*40 without a magnetic field (a,b) and in a magnetic field with in-plane (c,d) and out-plane (e,f) orientations of vector **B**. (For interpretation of the references to color in this figure legend, the reader is referred to the web version of this article.)

Growth of the thickness and change of structure of the *CBNL*40 sample due to an increase in growth time leads to a significant transformation of both the temperature and magnetic field dependences of the resistivity (conductivity). In particular, an increase in the thickness of the carbon sublayer in this sample allows the movement (deflection) of charge carriers in the direction perpendicular to its plane under the influence of Lorentz force in an in-plane oriented magnetic field, which leads to the action of the mechanism (III) manifested as the *PMR* effect. In addition, in this case, when measuring the temperature dependence of conductivity, in addition to the interference WL and activation contributions, the existence of three-dimensional quantum corrections to conductivity was also revealed.

It should be noted that the assumption of non-uniform (focused) distribution of magnetic flux Φ is a hypothesis, without which it is impossible, in our opinion, to consistently describe the entire complex of the above effects. We understand that this hypothesis requires experimental confirmation or refutation. To do this,we plan to subsequently measure the magnetic characteristics of the samples (study the dependences of magnetization on the magnetic field and temperature), to make magnetic force microscopy, to study the Hall effect, and conduct additional studies on a series of samples with a smaller step of growth time when occur the *VG* phase nucleation.

4. Conclusions

Structure and electrical properties of carbon-based nanolayers (*CBNL*) prepared by *PECVD* method on fused silica substrates were studied. Two series of samples have been grown at deposition time of 20 min (*CBNL*20) and 40 min (*CBNL*40). It was observed by Raman spectroscopy and scanning electron microscopy that the formed *CBNL* consist of a sublayer of graphite on substrate (with 20 and 35 nm thick for *CBNL*20 and *CBNL*40, respectively) covered with non-overlapping randomly distributed ellipse-like islands (nuclei) of future vertical graphene (*VG*) phase having mean values of long/short ellipse axes ~4.2/2.6 nm and ~10.5/6.1 nm and nuclei densities $\sim 2.5 \cdot 10^{10\prime}$ cm^{-2} and $\sim 5.4 \cdot 10^{9\prime}$ cm^{-2} for *CBNL*20 and *CBNL*40, respectively. On the samples obtained, the temperature dependences of the sheet electrical resistivity/conductivity $\rho(T,\mathbf{B})/\sigma(T,\mathbf{B})$ at $2 \le T \le 300$ K and magnetic fields $0 \le B \le 8$ *T* were studied.

It has been established that in the quasi-two-dimensional (2*D*) *CBNL*20 sample, two main mechanisms are responsible for $\sigma(T)$: 2*D* quantum corrections (*QCs*) to the Drude conductivity due to weak localization (*WL*) effects and the activation mechanism, which makes a noticeable contribution only at relatively high temperatures (150...300 K). With a perpendicular (out-plane) orientation of the **B** vector in this sample, 3 contributions to the magnetoresistance are observed: from the 2*D QCs* (I), from scattering by (para)magnetic inclusions and defects (II) and the Lorentz-like mechanism (III). The nature of mechanism (II) is most likely due to defects in the carbon structure like grain boundaries in the nanographite sublayer, dangling bonds at the interface between the graphite sublayer and the nuclei of the future *VG* phase and other paramagnetic centers with uncompensated spins. In the case of the in-plane oriented magnetic field, the QCs and the Lorentz mechanism of magnetoresistance $MR(B)$ do not appear in this sample due to the impossibility of deflecting charge carriers in the direction perpendicular to the sample plane due to lower thickness. At the same time, the mechanism of scattering by spins (II) is preserved.

An increase in the thickness of the carbon sublayer in the *CBNL*40 sample allows the movement (deflection) of carriers in the direction perpendicular to the sample plane under the influence of an in-plane oriented magnetic field, which leads to the manifestation of mechanism (III) in the form of the Lorentz *PMR* effect. Besides, when measuring the $\sigma_{\square}(T)$, in addition contributions from 2*D-WL* effect and the band (activation) mechanism of conductivity, we observed the appearance of the contribution from 3*D QCs*. We also note that the manifestation of the *NMR* effect associated with mechanism (II) is not observed of *CBNL*40, which is due to a decrease in the concentration of single paramagnetic centers between the *VG* phase islands. Another feature of the *CBNL*40 sample is that with a perpendicular orientation of the induction vector **B**, the dependence $MR(B)$ follow the theory of *QCs* (I) but in fields noticeably greater than those predicted by the Aronov–Altshuler theory and with greatly overestimated values of the parameter B_{φ}, which characterizes the phase breaking of the electron wave function during scattering.

To explain the observed inconsistencies between theory and experiments we propose a phenomenological model, which considers the evolution of the samples structure with growth of conductive graphite sub-layer thickness due to increasing *PECVD* deposition time. This evolution results in appearance of clusters with the enriched concentration of paramagnetic centers (and strong ferromagnetic moments, accordingly) under nuclei of *VG* phase in *CBNL*40 sample. These “magnetic” clusters in the *CBNL*40 sample result in concentration of magnetic flux Φ in island-like nuclei of *VG* phase. The described inhomogeneous distribution of the magnetic flux means that the islands and the parts of the nanographite sublayer between them are affected by magnetic fields of different magnitudes: enhanced magnetic field *B* over the *VG* phase islands (in the vicinity of these “magnetic” spin-enriched clusters with strong *M*) and weakened *B* values between the nuclei-islands of *VG*

phase. Such redistribution of magnetic field values among other things, manifests itself in the seeming displacement of the effect *NMR* from the *WL* contribution in the perpendicular field to the region of significantly larger fields and the lack of observation in our measurements of the *PMR* effect.

Thus, the article describes the main features of charge carrier transport in carbon structures obtained at the initial stages of growth of vertical graphene formed by *PECVD*. A possible explanation is given for the manifestation of the anomalous magnetoresistive effect (*AMR*) in external fields above 1 *T* in carbon materials. For the relatively thin sample *CBNL*20, *AMR* most likely involves scattering of charge carriers at magnetic centers. For *CBNL*40, we propose an alternative phenomenological explanation of the possible reason for the observation of the *NMR* effect in external fields above 1 T, formally described within the framework of the *WL* quantum corrections theory. Within the framework of this model, a non-uniform distribution of the magnetic flux density over the area of the sample is assumed: its concentration in the clusters of the carbon layer having strong magnetic moment (due to strong concentration of paramagnetic defects) and its sharp weakening between these clusters.

Declaration of competing interest

The authors declare the following financial interests/personal relationships which may be considered as potential competing interests: Andrei Kharchanka reports financial support was provided by State Program of Scientific Research of Republic of Belarus. If there are other authors, they declare that they have no known competing financial interests or personal relationships that could have appeared to influence the work reported in this paper.

Acknowledgments

The work was funded by State Program of Scientific Research of Republic of Belarus “Photonics and electronics for innovations”, 2021–2025, Subprogram “Micro- and nano-electronics”, contract No.. 20212560.

Appendix A. Supplementary data

Supplementary material related to this article can be found online at https://doi.org/10.1016/j.nxmate.2025.101081.

References

[1] Hiroshi Yaguchi, John Singleton, Destruction of the field-induced density-wave state in graphite by large magnetic fields, Phys. Rev. Lett. 81 (23) (1998) 5193, http://dx.doi.org/10.1103/PhysRevLett.81.5193.

[2] X. Zhang, Q.Z. Xue, D.D. Zhu, Positive and negative linear magnetoresistance of graphite, Phys. Lett. A 320 (5–6) (2004) 471–477, http://dx.doi.org/10.1016/j.physleta.2003.11.050.

[3] Y. Hishiyama, H. Irumano, Y. Kaburagi, Y. Soneda, Structure, Raman scattering, and transport properties of boron-doped graphite, Phys. Rev. B 63 (24) (2001) 245406, http://dx.doi.org/10.1103/PhysRevB.63.245406.

[4] Yutaka Kaburagi, Yoshihiro Hishiyama, Electronic properties of kish graphite crystals with low values of residual resistivity ratio, Carbon 36 (11) (1998) 1671–1676, http://dx.doi.org/10.1016/S0008-6223(98)00163-8.

[5] AI Romanenko, OB Anikeeva, AV Okotrub, LG Bulusheva, VL Kuznetsov, Yu V. Butenko, AL Chuvilin, C. Dong, Y. Ni, The temperature dependence of the electrical resistivity and the negative magnetoresistance of carbon nanoparticles, Phys. Solid State 44 (2002) 487–489, http://dx.doi.org/10.1134/1.1462682.

[6] Andrea C. Ferrari, Francesco Bonaccorso, Vladimir Fal'Ko, Konstantin S. Novoselov, Stephan Roche, Peter Bøggild, Stefano Borini, Frank HL Koppens, Vincenzo Palermo, Nicola Pugno, et al., Science and technology roadmap for graphene, related two-dimensional crystals, and hybrid systems, Nanoscale 7 (11) (2015) 4598–4810, http://dx.doi.org/10.1039/C4NR01600A.

[7] Subrata Ghosh, K. Ganesan, Shyamal R. Polaki, TR Ravindran, Nanda Gopala Krishna, M. Kamruddin, AK Tyagi, Evolution and defect analysis of vertical graphene nanosheets, J. Raman Spectrosc. 45 (8) (2014) 642–649, http://dx.doi.org/10.1002/jrs.4530.

[8] Mineo Hiramatsu, Hiroki Kondo, Masaru Hori, Graphene nanowalls, New Prog. Graphene Res. 10 (2013) 51528, http://dx.doi.org/10.5772/51528.

[9] Sanjay K. Behura, Indrajit Mukhopadhyay, Akira Hirose, Qiaoqin Yang, Omkar Jani, Vertically oriented few-layer graphene as an electron field-emitter, Phys. Status Solidi (A) 210 (9) (2013) 1817–1821, http://dx.doi.org/10.1002/pssa.201329172.

[10] Zengji Yue, Igor Levchenko, Shailesh Kumar, Donghan Seo, Xiaolin Wang, Shixue Dou, Kostya Ken Ostrikov, Large networks of vertical multi-layer graphenes with morphology-tunable magnetoresistance, Nanoscale 5 (19) (2013) 9283–9288, http://dx.doi.org/10.1039/C3NR00550J.

[11] Subrata Ghosh, K. Ganesan, SR Polaki, Tom Mathews, Sandip Dhara, M. Kamruddin, AK Tyagi, Influence of substrate on nucleation and growth of vertical graphene nanosheets, Appl. Surf. Sci. 349 (2015) 576–581, http://dx.doi.org/10.1016/j.apsusc.2015.05.038.

[12] Jiong Zhao, Mehrdad Shaygan, Jurgen Eckert, M. Meyyappan, Mark H. Rummeli, A growth mechanism for free-standing vertical graphene, Nano Lett. 14 (6) (2014) 3064–3071, http://dx.doi.org/10.1021/nl501039c.

[13] Rizwan Ur Rehman Sagar, Xiaozhong Zhang, Jimin Wang, Chengyue Xiong, Negative magnetoresistance in undoped semiconducting amorphous carbon films, J. Appl. Phys. 115 (12) (2014) 123708, http://dx.doi.org/10.1063/1.4869780.

[14] Xili Gao, Qingzhong Xue, Lanzhong Hao, Qun Li, Qingbin Zheng, Ping Tian, Effect of gas pressure on current-voltage characteristics of amorphous carbon film/silicon heterojunction, Appl. Phys. Lett. 91 (9) (2007) 092104, http://dx.doi.org/10.1063/1.2776017.

[15] Chang Hyun Lee, Koeng Su Lim, Boron-doped amorphous diamondlike carbon as a new p-type window material in amorphous silicon p-i-n solar cells, Appl. Phys. Lett. 72 (1) (1998) 106–108, http://dx.doi.org/10.1063/1.120659.

[16] P. Delhaes, Chemical vapor deposition and infiltration processes of carbon materials, Carbon 40 (5) (2002) 641–657, http://dx.doi.org/10.1016/S0008-6223(01)00195-6.

[17] Nikola Slepičková Kasálková, Petr Slepička, Václav Švorčík, Carbon nanostructures, nanolayers, and their composites, Nanomaterials 11 (9) (2021) 2368, http://dx.doi.org/10.3390/nano11092368.

[18] Anke Krueger, Carbon Materials and Nanotechnology, John Wiley & Sons, 2010.

[19] AK Fedotov, AA Kharchanka, UE Gumiennik, JA Fedotova, Ali Arash Ronassi, AS Fedotov, SL Prischepa, MV Chichkov, MD Malinkovich, Sheet resistance and magnetoresistance in polycrystalline CVD graphenes, Phys. Solid State 64 (7) (2022) 876–888, http://dx.doi.org/10.21883/PSS.2022.07.54598.321.

[20] Y. Kaburagi, Y. Hishiyama, Linear dependence of transverse magnetoresistance on magnetic field in kish graphite, Carbon 33 (10) (1995) 1505–1506, http://dx.doi.org/10.1016/0008-6223(95)96989-L.

[21] Y. Kaburagi, Y. Hishiyama, Anomalous hall coefficient in kish graphite, Carbon 33 (9) (1995) 1349–1350, http://dx.doi.org/10.1016/0008-6223(95)93956-M.

[22] Shigeji Fujita, Negative magnetoresistance in carbons and diffuse scattering at crystallite boundaries, Carbon 6 (5) (1968) 746–748, http://dx.doi.org/10.1016/0008-6223(68)90022-5.

[23] Elias Andrade, Florentino López-Urías, Gerardo G Naumis, Topological origin of flat bands as pseudo-Landau levels in uniaxial strained graphene nanoribbons and induced magnetic ordering due to electron-electron interactions, Phys. Rev. B 107 (23) (2023) 235143, http://dx.doi.org/10.1103/PhysRevB.107.235143.

[24] Chenxiao Zhao, Qiang Huang, Leoš Valenta, Kristjan Eimre, Lin Yang, Aliaksandr V. Yakutovich, Wangwei Xu, Ji Ma, Xinliang Feng, Michal Juríček, et al., Tailoring magnetism of graphene nanoflakes via tip-controlled dehydrogenation, Phys. Rev. Lett. 132 (4) (2024) 046201, http://dx.doi.org/10.1103/PhysRevLett.132.046201.

[25] Yositaka Yosida, Isamu Oguro, Variable range hopping conduction in multiwalled carbon nanotubes, J. Appl. Phys. 83 (9) (1998) 4985–4987, http://dx.doi.org/10.1063/1.367302.

[26] Y. Hishiyama, Negative magnetoresistance in soft carbons and graphite, Carbon 8 (3) (1970) 259–269, http://dx.doi.org/10.1016/0008-6223(70)90067-9.

[27] PM Vora, P. Gopu, M. Rosario-Canales, CR Pérez, Y. Gogotsi, JJ Santiago-Avilés, JM Kikkawa, Correlating magnetotransport and diamagnetism of sp2-bonded carbon networks through the metal-insulator transition, Phys. Rev. B 84 (15) (2011) 155114, http://dx.doi.org/10.1103/PhysRevB.84.155114.

[28] V. Prasad, S.V. Subramanyam, Magnetotransport in the amorphous carbon films prepared from succinic anhydride, Phys. B 369 (1–4) (2005) 168–176, http://dx.doi.org/10.1016/j.physb.2005.08.009.

[29] Caihua Wan, Xiaozhong Zhang, Johan Vanacken, Xili Gao, Xin Zhang, Lihua Wu, Xinyu Tan, Hong Lin, Victor V. Moshchalkov, Jun Yuan, Electro-and magneto-transport properties of amorphous carbon films doped with iron, Diam. Relat. Mater. 20 (1) (2011) 26–30, http://dx.doi.org/10.1016/j.diamond.2010.11.001.

[30] Yang-Bo Zhou, Bing-Hong Han, Zhi-Min Liao, Han-Chun Wu, Da-Peng Yu, From positive to negative magnetoresistance in graphene with increasing disorder, Appl. Phys. Lett. 98 (22) (2011) 222502, http://dx.doi.org/10.1063/1.3595681.

[31] Patrick A. Lee, T.V. Ramakrishnan, Disordered electronic systems, Rev. Modern Phys. 57 (2) (1985) 287, http://dx.doi.org/10.1103/RevModPhys.57.287.

[32] B.L. Al'Tshuler, A.G. Aronov, D.E. Khmel'Nitskiĭ, Negative magnetoresistance in semiconductors in the hopping conduction region, Sov. J. Exp. Theor. Phys. Lett. 36 (5) (1982) 195–198, URL http://jetpletters.ru/ps/0/article_20140.shtml.

[33] E. Abrahams, P.W. Anderson, D.C. Licciardello, T.V. Ramakrishnan, Scaling theory of localization: Absence of quantum diffusion in two dimensions, Phys. Rev. Lett. 42 (1979) 673, http://dx.doi.org/10.1103/PhysRevLett.42.673.

[34] Shinobu Hikami, Anatoly I. Larkin, Yosuke Nagaoka, Spin-orbit interaction and magnetoresistance in the two dimensional random system, Progr. Theoret. Phys. 63 (2) (1980) 707–710, http://dx.doi.org/10.1143/PTP.63.707.

[35] V. Bayev, M. Rybin, I. Svito, J. Przewoźnik, Cz Kapusta, J. Kasiuk, S. Vorobyova, A. Konakov, E. Obraztsova, The effect of quasi-free graphene layer on the electrical transport properties of sandwich-like graphene/Co nanoparticles/graphene structure, Appl. Surf. Sci. 579 (2022) 152119, http://dx.doi.org/10.1016/j.apsusc.2021.152119.

[36] Leizhi Wang, Ming Yin, Mohammed Abdi, Timir Datta, Linear magnetoresistance in three-dimensional carbon nanostructure with periodic spherical voids, Appl. Phys. Lett. 107 (2) (2015) 023103, http://dx.doi.org/10.1063/1.4926606.

[37] Alfred Brian Pippard, Magnetoresistance in Metals, vol. 2, Cambridge University Press, ISBN: 9780521118804, 1989.

[38] M.M. Parish, P.B. Littlewood, Non-saturating magnetoresistance in heavily disordered semiconductors, Nature 426 (6963) (2003) 162–165, http://dx.doi.org/10.1038/nature02073.

[39] Ferdinand Kisslinger, Christian Ott, Christian Heide, Erik Kampert, Benjamin Butz, Erdmann Spiecker, Sam Shallcross, Heiko B. Weber, Linear magnetoresistance in mosaic-like bilayer graphene, Nat. Phys. 11 (8) (2015) 650–653, http://dx.doi.org/10.1038/nphys3368.

[40] R. Xu, A. Husmann, TF Rosenbaum, M-L Saboungi, JE Enderby, PB Littlewood, Large magnetoresistance in non-magnetic silver chalcogenides, Nature 390 (6655) (1997) 57–60, http://dx.doi.org/10.1038/36306.

[41] M. Lee, T.F. Rosenbaum, M.-L. Saboungi, H.S. Schnyders, Band-gap tuning and linear magnetoresistance in the silver chalcogenides, Phys. Rev. Lett. 88 (6) (2002) 066602, http://dx.doi.org/10.1103/PhysRevLett.88.066602.

[42] A. Husmann, JB Betts, GS Boebinger, A. Migliori, TF Rosenbaum, M-L Saboungi, Megagauss sensors, Nature 417 (6887) (2002) 421–424, http://dx.doi.org/10.1038/417421a.

[43] Michael P. Delmo, Shinpei Yamamoto, Shinya Kasai, Teruo Ono, Kensuke Kobayashi, Large positive magnetoresistive effect in silicon induced by the space-charge effect, Nature 457 (7233) (2009) 1112–1115, http://dx.doi.org/10.1038/nature07711.

[44] NV Kozlova, N. Mori, O. Makarovsky, L. Eaves, QD Zhuang, Anthony Krier, A. Patanè, Linear magnetoresistance due to multiple-electron scattering by low-mobility islands in an inhomogeneous conductor, Nat. Commun. 3 (1) (2012) 1097, http://dx.doi.org/10.1038/ncomms2106.

[45] B.L. Altshuler, A.G. Aronov, A.I. Larkin, D.E. Khmelnitskii, Anomalous magnetoresistance in semiconductors, Sov. J. Exp. Theor. Phys. 54 (2) (1981) 411–419, URL http://www.jetp.ras.ru/cgi-bin/index/e/54/2/p411?a=list.

[46] T.A. Polyanskaya, Yu.V. Shmartsev, Quantum corrections to conductivity in semiconductors with two-dimensional and three-dimensional electron gas. Experiment, Sov. Phys. Semicond. 23 (1) (1989) 3–32.

[47] L.P. Gorkov, A.I. Larkin, D.E. Khmelnitsky, Particle conductivity in a two-dimensional random potential, Lett. JETF 30 (4) (1979) 228–232 (248), URL http://jetpletters.ru/ps/0/article_20629.shtml.

[48] Boris Isaakovich Shklovskii, Alex L. Efros, Electronic Properties of Doped Semiconductors, Springer Science & Business Media, 2013, http://dx.doi.org/10.1007/978-3-662-02403-4.

[49] B.I. Shklovskii, Hopping conduction in semiconductors subjected to a strong electric field, Sov. Phys. Semicond. 6 (12) (1973) 1964–1967.

[50] Nevill Francis Mott, Edward A. Davis, Electronic Processes in Non-Crystalline Materials, Oxford University Press, ISBN: 9780199645336, 2012.

[51] Sergey Vasilyevich Barabash, Topics in the Physics of Inhomogeneous Materials, The Ohio State University, 2003.

[52] Erika Rajackaitė, Domantas Peckus, Rimantas Gudaitis, Mindaugas Andrulevičius, Tomas Tamulevičius, Dmytro Volyniuk, Šarūnas Meškinis, Sigitas Tamulevičius, Transient absorption spectroscopy as a promising optical tool for the quality evaluation of graphene layers deposited by microwave plasma, Surf. Coat. Technol. 395 (2020) 125887, http://dx.doi.org/10.1016/j.surfcoat.2020.125887.

[53] Erika Rajackaitė, Domantas Peckus, Rimantas Gudaitis, Tomas Tamulevičius, Šarūnas Meškinis, Sigitas Tamulevičius, The evolution of properties with deposition time of vertical graphene nanosheets produced by microwave plasma-enhanced chemical vapor deposition, Surf. Interfaces 27 (2021) 101529, http://dx.doi.org/10.1016/j.surfin.2021.101529.

[54] Alexey A. Maximenko, Erika Rajackaite, Sarunas Meskinis, Tomas Tamulevicius, Sigitas Tamulevicius, Andrei A. Kharchanka, Alexander K. Fedotov, Julia A. Fedotova, Electrical transport properties of a carbon nanostructure obtained by plasma-enhanced chemical vapor deposition during thermal cycling, J. Belarusian State Univ. 10 (3) (2020) 86–89, http://dx.doi.org/10.33581/2520-2243-2020-3-89-96.

[55] Yu.A. Fedotova, A.A. Kharchenko, A.K. Fedotov, M.V. Chichkov, M.D. Malinkovich, A.O. Konakov, S.A. Vorobyova, Yu.V. Kasyuk, V.E. Gumennik, A.A. Maksimenko, Effect of magnetic Co–CoO particles on the carrier transport in monolayer graphene, Phys. Solid State 62 (2020) 368–377.

[56] A.S. Fedotov, V.G. Shepelevich, I.A. Svito, V.A. Sivakov, Temperature dynamics of the electronic structure in dilute Bi-Sn alloys, Phys. Rev. B 97 (7) (2018) 075204, http://dx.doi.org/10.1103/PhysRevB.97.075204.

[57] B.I. Shklovsky, A.L. Efros, Electronic Properties of Doped Semiconductors, Moscow, Izdatel'stvo Nauka, 1979.

[58] P.W. Anderson, E. Abrahams, T.V. Ramakrishnan, Possible explanation of nonlinear conductivity in thin-film metal wires, Phys. Rev. Lett. 43 (10) (1979) 718, http://dx.doi.org/10.1103/PhysRevLett.43.718.

[59] Elihu Abrahams, P.W. Anderson, P.A. Lee, T.V. Ramakrishnan, Quasiparticle lifetime in disordered two-dimensional metals, Phys. Rev. B 24 (12) (1981) 6783, http://dx.doi.org/10.1103/PhysRevB.24.6783.

[60] V.M. Pudalov, Metallic conduction, apparent metal-insulator transition and related phenomena in two-dimensional electron liquid, Proc. Int. Sch. Phys. "Enrico Fermi" 157 (2004) 335, http://dx.doi.org/10.3254/978-1-61499-013-0-335.

[61] Edward McCann, K. Kechedzhi, Vladimir I. Fal'ko, H. Suzuura, T. Ando, BL Altshuler, Weak-localization magnetoresistance and valley symmetry in graphene, Phys. Rev. Lett. 97 (14) (2006) 146805, http://dx.doi.org/10.1103/PhysRevLett.97.146805.

[62] Ö Mermer, G. Veeraraghavan, TL Francis, Y. Sheng, DT Nguyen, M. Wohlgenannt, Anna Köhler, Mohammed K. Al-Suti, Muhammad S. Khan, Large magnetoresistance in nonmagnetic π-conjugated semiconductor thin film devices, Phys. Rev. B 72 (20) (2005) 205202, http://dx.doi.org/10.1103/PhysRevB.72.205202.

[63] PA Bobbert, TD Nguyen, FWA Van Oost, van B. Koopmans, M. Wohlgenannt, Bipolaron mechanism for organic magnetoresistance, Phys. Rev. Lett. 99 (21) (2007) 216801, http://dx.doi.org/10.1103/PhysRevLett.99.216801.

[64] T.D. Nguyen, Y. Sheng, J. Rybicki, M. Wohlgenannt, Magnetic field-effects in bipolar, almost hole-only and almost electron-only tris-(8-hydroxyquinoline) aluminum devices, Phys. Rev. B 77 (23) (2008) 235209, http://dx.doi.org/10.1103/PhysRevB.77.235209.

[65] Y. Sheng, TD Nguyen, G. Veeraraghavan, Ö Mermer, M. Wohlgenannt, S. Qiu, U. Scherf, Hyperfine interaction and magnetoresistance in organic semiconductors, Phys. Rev. B 74 (4) (2006) 045213, http://dx.doi.org/10.1103/PhysRevB.74.045213.

[66] V.N. Prigodin, J.D. Bergeson, D.M. Lincoln, A.J. Epstein, Anomalous room temperature magnetoresistance in organic semiconductors, Synth. Met. 156 (9–10) (2006) 757–761, http://dx.doi.org/10.1016/j.synthmet.2006.04.010.

[67] Nobuo Mikoshiba, Shun-ichi Gonda, Weak-field magnetoresistance of impurity conduction in n-type germanium, Phys. Rev. 127 (6) (1962) 1954, http://dx.doi.org/10.1103/PhysRev.127.1954.

[68] B. Movaghar, L. Schweitzer, A model for the anomalous magnetoresistance in amorphous semiconductors, J. Phys. C: Solid State Phys. 11 (1) (1978) 125, http://dx.doi.org/10.1088/0022-3719/11/1/023.

[69] Atsushi Kurobe, Hiroshi Kamimura, Theory of magnetoresistance in amorphous semiconductors, J. Non-Cryst. Solids 59–60 (1) (1983) 41–44.

[70] Alexandre S. Alexandrov, Valentin A. Dediu, Victor V. Kabanov, Hopping magnetotransport via nonzero orbital momentum states and organic magnetoresistance, Phys. Rev. Lett. 108 (18) (2012) 186601, http://dx.doi.org/10.1103/PhysRevLett.108.186601.

[71] Hidetoshi Fukuyama, Kei Yosida, Negative magnetoresistance in the Anderson localized states, J. Phys. Soc. Japan 46 (1) (1979) 1522–1528, http://dx.doi.org/10.1143/JPSJ.46.1522.

[72] Boris L. Altshuler, A.G. Aronov, D.E. Khmelnitsky, Effects of electron-electron collisions with small energy transfers on quantum localisation, J. Phys. C: Solid State Phys. 15 (36) (1982) 7367, http://dx.doi.org/10.1088/0022-3719/15/36/018.

[73] T.F. Rosenbaum, K. Andres, G.A. Thomas, P.A. Lee, Conductivity cusp in a disordered metal, Phys. Rev. Lett. 46 (8) (1981) 568.

[74] Andrew J. Millis, Peter B. Littlewood, Boris I. Shraiman, Double exchange alone does not explain the resistivity of La(1-x)Sr(x) MnO(3), Phys. Rev. Lett. 74 (25) (1995) 5144, http://dx.doi.org/10.1103/PhysRevLett.74.5144.

[75] A.J. Millis, Boris I. Shraiman, R. Mueller, Dynamic jahn-teller effect and colossal magnetoresistance in La(1- x)Sr(x)MnO(3), Phys. Rev. Lett. 77 (1) (1996) 175, http://dx.doi.org/10.1103/PhysRevLett.77.175.

[76] A.S. Alexandrov, A.M. Bratkovsky, Carrier density collapse and colossal magnetoresistance in doped manganites, Phys. Rev. Lett. 82 (1) (1999) 141, http://dx.doi.org/10.1103/PhysRevLett.82.141.

[77] Abdelghani Sybous, Abdelhamid El Kaaouachi, Abdelfattah Narjis, Lhoussine Limouny, Said Dlimi, Gerard Biskupski, Negative magnetoresistance behaviour and variable range hopping conduction in insulating NbSi amorphous alloys at very low temperature with magnetic field, J. Mod. Phys. 3 (7) (2012) 521–528, http://dx.doi.org/10.4236/jmp.2012.37071, SPIE.

[78] Yutaka Toyozawa, Theory of localized spins and negative magnetoresistance in the metallic impurity conduction, J. Phys. Soc. Japan 17 (6) (1962) 986–1004, http://dx.doi.org/10.1143/JPSJ.17.986.

[79] Kei Yosida, Anomalous electrical resistivity and magnetoresistance due to an s-d interaction in Cu-Mn alloys, Phys. Rev. 107 (2) (1957) 396, http://dx.doi.org/10.1103/PhysRev.107.396.

[80] Rui Sakano, Tokuro Hata, Kaiji Motoyama, Yoshimichi Teratani, Kazuhiko Tsutsumi, Akira Oguri, Tomonori Arakawa, Meydi Ferrier, Richard Deblock, Mikio Eto, et al., Kondo temperature evaluated from linear conductance in magnetic fields, Phys. Rev. B 108 (20) (2023) 205147, http://dx.doi.org/10.1103/PhysRevB.108.205147.

[81] B. Raquet, M. Viret, E. Sondergard, O. Cespedes, R. Mamy, Electron-magnon scattering and magnetic resistivity in 3 d ferromagnets, Phys. Rev. B 66 (2) (2002) 024433, http://dx.doi.org/10.1103/PhysRevB.66.024433.

[82] F.V. Tikhonenko, A.A. Kozikov, A.K. Savchenko, R.V. Gorbachev, Transition between electron localization and antilocalization in graphene, Phys. Rev. Lett. 103 (22) (2009) 226801, http://dx.doi.org/10.1103/PhysRevLett.103.226801.

[83] NA Poklonski, AN Dzeraviaha, SA Vyrko, AG Zabrodskii, AI Veinger, PV Semenikhin, Curie–weiss behavior of the low-temperature paramagnetic susceptibility of semiconductors doped and compensated with hydrogen-like impurities, AIP Adv. 11 (5) (2021) 055016, http://dx.doi.org/10.1063/5.0048886.

[84] Koichi Kusakabe, Masanori Maruyama, Magnetic nanographite, Phys. Rev. B 67 (9) (2003) 092406, http://dx.doi.org/10.1103/PhysRevB.67.092406.

[85] Elizabeth J. Duplock, Matthias Scheffler, Philip J.D. Lindan, Hallmark of perfect graphene, Phys. Rev. Lett. 92 (22) (2004) 225502, http://dx.doi.org/10.1103/PhysRevLett.92.225502.

[86] Oleg V. Yazyev, Lothar Helm, Defect-induced magnetism in graphene, Phys. Rev. B 75 (12) (2007) 125408, http://dx.doi.org/10.1103/PhysRevB.75.125408.

[87] Hideki Kumazaki, Dai S. Hirashima, Nonmagnetic-defect-induced magnetism in graphene, J. Phys. Soc. Japan 76 (6) (2007) 064713, http://dx.doi.org/10.1143/JPSJ.76.064713.

[88] J. Červenka, CFJ Flipse, Structural and electronic properties of grain boundaries in graphite: planes of periodically distributed point defects, Phys. Rev. B 79 (19) (2009) 195429, http://dx.doi.org/10.1103/PhysRevB.79.195429.

[89] Chunli Huang, Tobias MR Wolf, Wei Qin, Nemin Wei, Igor V. Blinov, Allan H. MacDonald, Spin and orbital metallic magnetism in rhombohedral trilayer graphene, Phys. Rev. B 107 (12) (2023) L121405, http://dx.doi.org/10.1021/acs.jpclett.5c00614.

[90] P. Esquinazi, Handbook of magnetism and advanced magnetic materials, vol. 4, 2007, pp. 2256–2281, http://dx.doi.org/10.1002/9780470022184.

[91] T.L. Makarova, Magnetic properties of carbon structures, Semiconductors 38 (2004) 615–638, http://dx.doi.org/10.1134/1.1766362.

[92] Miguel M. Ugeda, Iván Brihuega, Francisco Guinea, José M. Gómez-Rodríguez, Missing atom as a source of carbon magnetism, Phys. Rev. Lett. 104 (9) (2010) 096804, http://dx.doi.org/10.1103/PhysRevLett.104.096804.

[93] J. Červenka, M.I. Katsnelson, CFJ Flipse, Room-temperature ferromagnetism in graphite driven by two-dimensional networks of point defects, Nat. Phys. 5 (11) (2009) 840–844, http://dx.doi.org/10.1038/nphys1399.

[94] N. Tang, T. Tang, H. Pan, Yu Sun, J. Chen, Y. Du, Chapter 6 – magnetic properties of graphene, Spintron. 2D Mater. Fundam. Appl. (2020) 137–161, http://dx.doi.org/10.1016/B978-0-08-102154-5.00005-9.

[95] Ziying Li, Shuilin Li, Jiawei Liu, Liang Zhou, Rui Liang, Fuchi Liu, Nujiang Tang, Realization of near-room-temperature superparamagnetism in graphene quantum dots by high-concentration semi-ionic fluorine functionalization, J. Phys. Chem. Lett. 16 (20) (2025) 4875–4882, http://dx.doi.org/10.1021/acs.jpclett.5c00614.

[96] Ziying Li, Shuilin Li, Yongjie Xu, Nujiang Tang, Recent advances in magnetism of graphene from 0D to 2D, Chem. Commun. 59 (42) (2023) 6286–6300, http://dx.doi.org/10.1039/D3CC01311A.

[97] Gaojie Zhang, Hao Wu, Li Yang, Wen Jin, Wenfeng Zhang, Haixin Chang, Graphene-based spintronics, Appl. Phys. Rev. 11 (2) (2024) http://dx.doi.org/10.1063/5.0191362.

[98] Kenji Kamishima, Miyata Daisuke, Sato Yūki, Tokue Takashi, Kakizaki Koichi, Hiratsuka Nobuyuki, Imanaka Yasutaka, Takamasu Tadashi, Preparation of pyrolytic magnetic carbon under magnetic field, J. Phys. Conf. Ser. 200 (2010) 112003, http://dx.doi.org/10.1088/1742-6596/200/11/112003.

[99] Man Zhao, He Xiao, Shuai Chen, Tianjun Hu, Jianfeng Jia, Haishun Wu, Temperature-tuned ferromagnetism in hydrogenated multilayer graphene, RSC Adv. 8 (24) (2018) 13148–13153, http://dx.doi.org/10.1039/C8RA02648C.

[100] J. Samuel Smart, The Néel theory of ferrimagnetism, Am. J. Phys. 23 (6) (1955) 356–370, http://dx.doi.org/10.1119/1.1934006.

[101] Ping-Zhan Si, Hui-Dong Qian, Hong-Liang Ge, Jihoon Park, Chul-Jin Choi, Enhancing the magnetization of Mn4C by heating, Appl. Phys. Lett. 112 (19) (2018) 192407, http://dx.doi.org/10.1063/1.5023840.

[102] Andrei A. Kharchenko, Julia A. Fedotova, Valeryia Yu Slabukho, Alexander K. Fedotov, Alexey V. Pashkevich, Ivan A. Svito, Maxim V. Bushinsky, Electrical and galvanomagnetic properties of black phosphorus single crystals, Mod. Electron. Mater. 7 (4) (2021) 127–139, http://dx.doi.org/10.3897/j.moem.7.4.78587.

[103] LX Zhang, Z. Sun, J. Lv Qi, JM Shi, TD Hao, JC Feng, Understanding the growth mechanism of vertically aligned graphene and control of its wettability, Carbon 103 (2016) 339–345, http://dx.doi.org/10.1016/j.carbon.2016.03.029.

[104] Yifei Ma, Haegyu Jang, Sun Jung Kim, Changhyun Pang, Heeyeop Chae, Copper-assisted direct growth of vertical graphene nanosheets on glass substrates by low-temperature plasma-enhanced chemical vapour deposition process, Nanoscale Res. Lett. 10 (2015) 308, http://dx.doi.org/10.1186/s11671-015-1019-8.